International Journal of Hydrogen Energy 249 (2026) 155963

Contents lists available at ScienceDirect

International Journal of Hydrogen Energy

journal homepage: www.elsevier.com/locate/he

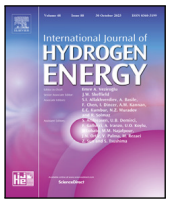

A discontinuity-capturing approach to the simulation of two-phase hydrogen flows

Nicolás Capmany [a], László Könözsy [b,*], Drewan Sanders [a]

[a] Centre for Aeronautics, Propulsion and Power, Cranfield University, Cranfield, Bedfordshire, MK43 0AL, United Kingdom
[b] Centre for Assured and Connected Autonomy, Cranfield University, Cranfield, Bedfordshire, MK43 0AL, United Kingdom

ARTICLE INFO

Keywords:
Liquid hydrogen
Pipeline
Hydrogen infrastructure
Two-phase flows
Homogeneous equilibrium
Computational fluid dynamics

ABSTRACT

This paper focuses on the development of a Godunov-type approach in the context of two-phase liquid hydrogen (LH_2) flows for pipeline networks, implemented and verified in an in-house code. The motivation of this work is to overcome the uncertainties arising in the numerical prediction of thermo-fluid hydrogen dynamics due to its extreme properties at low temperatures. It has been found that the Godunov-type approach developed here reduces the average relative error to 1.90% compared to well-established benchmark problems for compressible fluid flows, including a case with a non-linear boundary condition treatment. The selected examples have industrial relevance for cryogenic management systems. The obtained numerical results provide a reference solution for two-phase hydrogen flows. They also suggest that this variant of the Godunov-type method could serve as a suitable solution to enhance the accurate prediction of thermo-fluid hydrogen dynamics and support the design process of LH_2 infrastructure for net-zero aviation.

1. Introduction

1.1. LH_2 in civil aviation: the challenge of cryogenic hydrogen flows

In the context of a decarbonising economy, hydrogen (H_2) has attracted attention of industry stakeholders for its potential to deliver large energy outputs with zero carbon emissions. As a result, the aerospace and defence sectors seek to optimise space and weight by using LH_2 to propel their fleets, triggering research efforts to understand the implications of LH_2 as an energy carrier. Initial studies focused on its broader implications. Verstraete [1], for example, investigated hydrogen propulsion integration across different technology levels, as well as quantified performance penalties on aircraft with varying passenger capacity [2]. Following studies focused on targeted challenges, as it is the case of LH_2 storage. In this context, Huete and Pilidis [3] examined cryogenic tank integration strategies for civil aircraft, whereas Rompokos et al. [4] developed a modelling framework for structural sizing of LH_2 tank walls under cryogenic operating conditions. Moving beyond storage alone, work was also devoted to understanding the design of fuel delivery systems. In this regard, Stroman et al. [5] analysed the architectural design of LH_2 fuel systems for military unmanned aircraft, and Ebrahimi et al. [6] provided a comprehensive review of state-of-the-art LH_2 fuel system configurations for civil aviation. Although these contributions primarily address system-level architecture and design integration, their findings implicitly highlight the increasing relevance of characterising the thermo-fluid behaviour of internal LH_2 flows. LH_2, however, is a cryogen, and has a fundamentally different behaviour from standard engineering fluids (e.g. oil blends, water or air) [7]. Cryogenic fluids are notably sensitive to small heat leaks, as well as showing a large temperature difference with ambient conditions. Consequently, it is usually the case that LH_2 will exhibit transient two-phase conditions when pumped through pipeline systems.

Two-phase phenomena introduce significant challenges in the design of fuel delivery systems. Hydraulic components — including pumps, valves, flowmeters, and heat exchangers — are affected by the unsteady nature of the flow, which can lead to performance limitations. Pumps, for instance, often operate with fluids near saturation, leaving virtually no net-positive suction head (NPSH) [8], while effects such as liquid compressibility and cavitation onset can readily induce surge conditions [9,10]. Valves and flowmeters similarly struggle to maintain stable operation, as vapour bubble formation triggers oscillations and pressure drops that compromise metering accuracy [11,12]. Additional evidence across different valve applications — including safety relief [13,14], metering [15], and pump valves [16] — further

* Corresponding author.
E-mail address: laszlo.konozsy@cranfield.ac.uk (L. Könözsy).

https://doi.org/10.1016/j.ijhydene.2026.155963
Received 24 January 2026; Received in revised form 20 May 2026; Accepted 6 June 2026
Available online 15 June 2026
0360-3199/© 2026 The Authors. Published by Elsevier Ltd on behalf of Hydrogen Energy Publications LLC. This is an open access article under the CC BY license (http://creativecommons.org/licenses/by/4.0/).

Nomenclature

0-D	Zero-dimensional
1-D	One-dimensional
BC	Boundary condition
CFD	Computational fluid dynamics
CH_4	Methane
EoS	Equation of state
FVM	Finite volume method
GCI	Grid convergence index
H_2	Hydrogen
H_2O	Water
HEM	Homogeneous equilibrium model
LH_2	Liquid hydrogen
LHS	Left-hand side
N_2	Nitrogen
NPSH	Net-positive suction head
$N\text{-}H_2$	Normal hydrogen
$O\text{-}H_2$	Orthohydrogen
$P\text{-}H_2$	Parahydrogen
RHS	Right-hand side

Symbols

A	Helmholtz free energy, J
D	Pipe diameter, m
E	Total energy, J/m^3
P	Static pressure, Pa
Q	Mass fraction, –
Re	Reynolds number, –
S_f	Frictional source term, m/s^2
S_h	Heat transfer source term, J/kg-s
T	Static temperature, K
V	Volume, m^3
c	Speed of sound, m/s
e	Specific internal energy, J/kg
f	Darcy friction factor, –
h	Specific enthalpy, J/kg
h	Specific enthalpy, J/kg
s	Specific entropy, J/kg
t	Temporal coordinate, s
u	Flow velocity, m/s
x	Spatial coordinate, m

Greek Letters

α	Volume fraction, –
ϵ	Surface roughness, m
λ	Wave speed, m/s
ρ	Density, kg/m^3
σ	Surface tension, N/m

Superscripts

$\circ$	Ideal
r	Residual
$\hat{}$	Roe-averaged quantity
$*$	Sonic conditions

Subscripts

atm	Atmospheric
c	Critical point
gas	Gaseous phase
liq	Liquid phase
m	Homogeneous mixture
out	Pipe outlet
x	x-direction

highlights the sensitivity of these components to two-phase effects. Heat exchangers must also contend with shifting flow regimes and variable heat transfer coefficients, which reduce their overall efficiency [17,18].

Collectively, these examples underscore the strong dependence of component performance on two-phase dynamics and highlight the importance of accurately predicting the underlying physics. In particular, transient boiling and condensation fronts giving rise to sharp variations in void fraction, pressure, and mass flow rate. Said variations can lead to system-wide flow instabilities [19], as it has been commonly observed in processes such as chill-down (or pipe quenching) [20,21] and cryogenic cavitation [22,23]. Additionally, recent investigations of chill-down dynamics using nitrogen [24,25] and hydrogen [26,27] further confirm the complexity of cryogenic transients. These processes belong to a broader class of two-phase transients encountered in practical operations, including engine start-up, tank feed switching, and ground refuelling. Developing modelling capabilities that capture these intricate flow dynamics is therefore essential for advancing the design and operation of net-zero fuel delivery systems, as well as supporting progress towards higher technology readiness levels.

1.2. Simulation of LH_2 pipe flows: state of the art

Industrial workflows approach the design of fluid management systems using system-level software underpinned by low-fidelity models (i.e. 0-D and 1-D). They offer a rapid, yet comprehensive way to assess compliance of highly-integrated pipeline infrastructure. Although said tools often provide sufficient accuracy across a range of applications, they show limited capability in two-phase flow conditions; more precisely when the aim is to reproduce the physical behaviour of the flow. Shortcomings are most apparent in tools relying on 0-D models, as these omit coupling effects between momentum and energy terms. Siemens Simcenter Amesim [28,29] –being grounded in bond-graph theory [30]–exemplifies this approach. While it can reproduce integral flow metrics such as pressure losses and fuel consumption for hardware cooldown,[1] it does not resolve the transient evolution of flow properties during two-phase events.

1-D frameworks, on the other hand, capture momentum–energy coupling, but have been mainly applied to liquid rocket propulsion applications–where systems operate under different conditions from those of civil aviation. Rocket fuel architectures handle higher mass flow rates (40–300 kg/s), compared with conventional aircraft fuel systems (0.05–0.1 kg/s), and their mission profile spans only minutes, in contrast to the hours (or days) required in civil airframes. Furthermore, the thermodynamic cycles differ significantly, with rocket engines demanding combustion pressures and temperatures well above those of civil aircraft. Fig. 1 illustrates concisely the design space difference between both applications according to Falsetti [31].

Setting aside differences in scope, a number of one-dimensional (1-D) simulation suites are available, most of which are distinguished

[1] Applies to versions 2023 and later.

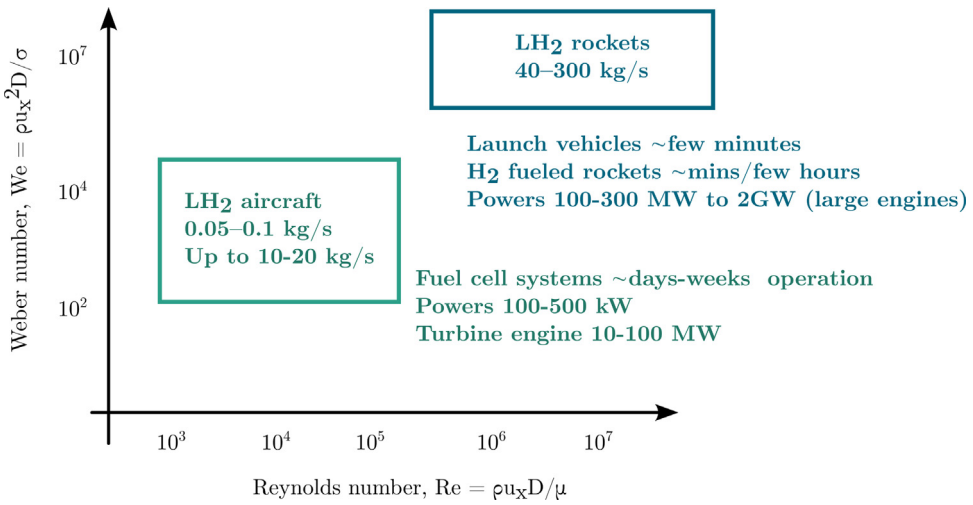

Fig. 1. Design space difference between liquid rocket propulsion systems and civil aviation fuel systems [31].

by the numerical schemes employed to solve the governing equations. A substantial subset of these tools has been applied to the modelling of chill-down processes; however, validation efforts have largely been limited to pipe-wall temperature measurements, and no comprehensive comparison against flow data has been reported to date. NASA GFSSP [32,33], for example, integrates pressure-based finite volume methods (FVMs) with fluid network analysis [34,35] but this approach, while versatile, has limitations [36,37]. It relies on equations of state derived from compressibility factors, diminishing the accuracy achievable with state-of-the-art thermophysical models [38–41]. Additionally, the fluid-network analysis framework underlying GFSSP restricts the adoption of updated heat-transfer correlations. It continues to rely on the Miropolskii correlation for flow boiling in water [42], rather than leveraging more recent works by Hartwig et al. [43,44], Shirai et al. [45], or Sakamoto et al. [46,47] stemming from LH_2 experiments. Such studies have led to the development of empirical correlations for the heat transfer coefficient in LH_2 flows [48–50], as well as investigations of chill-down processes under on-Earth conditions [51], yet none of these findings are currently implemented in GFSSP.

Another case is that of EcoSimPro/ESPSS, a library that can apply FVMs ranging from pressure- to shock-capturing schemes FVMs [52]. Amongst the latter figure Roe's method [53] and the AUSM schemes [54,55], both examples of flux vector splitting methods that can work with two-phase compressible flows. Roe's approach, nevertheless, is known to be non-entropy satisfying and omits solving the nonlinear problem described by the conservation equations of the flow [56]. AUSM schemes, on the other hand, can be applied in multiphase flow contexts, but their resolution of contact discontinuities–which are of interest in two-phase flow modelling–is limited [57]. ESPSS has been previously assessed in the context of liquid-rocket applications, with emphasis on predicting chill-down times and capturing the physics of cryogenic flows. Raia [58] evaluated the performance of ESPSS in modelling pipeline chill-down with different fluids, including LH_2. Findings suggested that while the tool could estimate pipe cooldown times with reasonable accuracy, it was unfit to fully capture the underlying fluid dynamics, as seen from its limited ability to predict mass flow and temperature trends under subcooled liquid conditions. It is worth noting that, when compared with the experimental measurements of Rame et al. [43], Raia assumes a pipe-wall thickness that is two orders of magnitude greater than that of the actual test setup, suggesting ESPSS might be even more constrained than initially thought. Raia's analysis, however, does not specify the numerical schemes used in ESPSS, leaving the performance of its shock-capturing methods unclear. Other studies, including those by Lema [59] and Porca et al. [60], assessed ESPSS capabilities when modelling different two-phase flow phenomena, particularly fluid-hammer events with gas desorption effects. Their analyses revealed limitations in the solver's predictive capability. Both works reported systematic pressure overprediction linked to steady friction models, while Lema also identified discrepancies between numerical and experimental pressures caused by inaccurate speed-of-sound estimations. These findings, nonetheless, were derived exclusively from test cases using water and ethanol, which are not representative of the conditions encountered in cryogenic fluid-management systems. Lema [59] compared the numerical schemes available at the time, including a centred differencing scheme and a first-order Roe upwind scheme, and selected the former due to its lower computational cost, despite its limited capability to resolve flow discontinuities.

In the academic literature, Luchinskiy et al. [61,62] applied the semi-implicit FVM method of Liles and Reed [63] to a separated-flow model, relying — as in the case of GFSSP — on pressure-velocity coupling algorithms [64,65]. Additional evidence can be found in subsequent studies [66,67]. Their validation was also limited to the same wall temperature data as in GFSSP [34,36], offering no insight into the flow itself. Using a different approach, Kuniyoor et al. [68] solved 1-D models by coupling an inverse method of characteristics with a Crank–Nicholson scheme [69]. While the framework was also validated against transient wall-temperature data [20], it similarly provided no evaluation of the underlying flow physics.

Building on the examples discussed earlier, and from a numerical analysis standpoint, tools implementing FVMs have commonly applied pressure-based methods to solve the 1-D flow conservation equations in a cryogenic context, leaving shock-capturing strategies comparatively underexplored. This is most apparent in the context of LH_2 flows, as there is little evidence on their application to transient two-phase phenomena in cryogenic liquids. While previous research has made clear efforts to model processes in low-temperature systems, the resulting insights are often limited to validation against hardware data, obviating flow behaviour, and with little to no detail on the numerical solution strategies employed.

1.3. Objectives of the present work

Computational fluid dynamics (CFD) schemes based on the FVM discretise the flow field as cell-averaged quantities. In first-order formulations, the solution is reconstructed as piecewise constant within each cell, leading to discontinuities at cell interfaces. These discontinuities define local Riemann problems, whose solutions describe the propagation of information through waves (i.e. shocks, rarefactions, and contact discontinuities). The resulting wave structure provides

physically consistent intercell fluxes, which are used to update the solution in time and are central to achieving high physical accuracy. Godunov-type methods [70] compute these fluxes by solving (exactly or approximately) the associated Riemann problems, thereby embedding the underlying flow physics directly into the numerical scheme. As a result, they capture discontinuities more sharply and robustly than conventional central or upwind methods, while preserving correct wave speeds and avoiding common numerical instabilities.

The relevance of such shock-capturing approaches is further supported by experimental observations in LH_2 flows, where sharp and often discontinuous variations in flow properties are frequently reported. In particular, Hartwig et al. [48,49] and Darr et al. [50], in the context of convective heat transfer correlations, document pronounced variations across different flow regimes. Similarly, Sakamoto et al. [46,47] report abrupt changes in void fraction behaviour, while earlier work by Shirai et al. [45] further confirms the presence of strong gradients and rapid thermofluid transitions. These observations highlight the potential benefits of applying shock-capturing schemes to LH_2 flows.

Within this class of methods, Godunov-type schemes have a well-established capability to resolve inviscid compressible flows and abrupt variations in flow properties [71,72]. Furthermore, their applicability extends beyond purely inviscid regimes, as demonstrated by their successful use in channel flows [73], mixed flows [74,75], and magnetohydrodynamics [76]. This broader range of applications suggests that such methods may also be well suited to modelling rapid phase-change phenomena in highly non-ideal fluids, thereby motivating their use in the present study.

This work represents the first effort to apply Godunov-type methods to reduced-order (i.e. 1-D) models for LH_2 two-phase flows in pipelines through the in-house code, `Arpad`. By assessing its ability to describe flow discontinuities and phase-change dynamics, the study contributes to a broader understanding of Godunov schemes and their applicability to the system-wide modelling of LH_2 transfer systems. In such infrastructure, two-phase flow behaviour may arise under a range of operational scenarios, including ground refuelling, engine start-up/shutdown, and tank feed switching in multi-tank aircraft configurations. The development of reduced-order framework grounded in Godunov's approach aims to reduce uncertainty in cryogenic management system design and operation, thereby contributing to civil aviation efforts towards net-zero emissions and sustainable flight.

2. Physical and mathematical modelling of two-phase hydrogen dynamics

The present section introduces the numerical framework for simulating two-phase hydrogen flows in pipelines. The model employs a homogeneous equilibrium model (HEM) formulation coupled with a multiparametric EoS developed for P-H_2 [77], representing an application not previously reported in the literature. HEMs are not generally suitable for capturing the detailed flow physics of transitioning flow boiling regimes as it may happen during two-phase processes. However, evidence from experimental studies conducted by Hartwig et al. [44,78] suggests that under certain conditions (i.e., hydrogen flow boiling at high Reynolds numbers within the transition and nucleate boiling regimes) may reasonably be approximated as homogeneous owing to the enhanced mixing observed. One can consider that the slip velocity, which is the ratio of the gas to liquid velocity should be approximately equal to unity justifying quantitatively the use of HEMs as suggested by Wallis [79]. Further details on this subject can be found in the book of Ishii and Hibiki [80]. The following subsections outline the model assumptions, governing equations, and thermodynamic closure approach.

2.1. The homogeneous equilibrium flow model

HEMs are widely adopted strategies for describing two-phase flows when the constitutive phases are sufficiently well mixed [79,81]. In this framework, the flow is represented as a single-phase mixture whose properties are averaged and updated based on its thermodynamic state. A HEM rests on three main assumptions:

1. Both phases are in thermodynamic equilibrium (i.e., $P_{gas}, T_{gas} = P_{liq}, T_{liq}$), implying instantaneous heat and mass transfer between them.
2. The phases have no relative motion, meaning a single mixture velocity is used.
3. The mixture properties are averaged according to the volume fraction of the gaseous phase (α), determined via an EoS relating pressure, temperature and density.

By treating two-phase mixtures as a homogeneous continuum, HEMs resolve the flow as a volume-weighted blend of the gas and liquid phase (see Fig. 2). Their distribution is characterised through the volume fraction (α), a dimensionless parameter defined as the ratio of the volume of gas to the volume of the whole fluid mixture:

$$\alpha = \frac{V_{gas}}{V_{gas} + V_{liq}} \,. \tag{1}$$

Volume fraction is a key determinant of HEM robustness because it is the main weighting factor updating the mixture properties. Consequently, using a state-of-the-art EoS is essential for achieving accurate predictions. A multiparametric EoS is employed in the current work, as it enables: (1) accurate approximations in the critical region, (2) estimation of saturated properties, and (3) definition of properties within the vapour dome. Through these advanced EoSs, the volume fraction (α) is obtained and subsequently used to update the mixture density (ρ_m).

$$\rho_m = \alpha \cdot \rho_{gas} + (1-\alpha) \cdot \rho_{liq} \,, \tag{2}$$

where ρ_{gas} and ρ_{liq} are the saturated gas and liquid densities for a specific thermodynamic state. HEMs allow simplifying the problem to a single set of conservation laws. To remain consistent with the 1-D framework needed for system-level simulations, the governing equations are expressed as:

$$\frac{\partial \rho_m}{\partial t} = -\frac{\partial (\rho_m u_x)}{\partial x} \,, \tag{3}$$

$$\frac{\partial (\rho_m u_x)}{\partial t} = -\frac{\partial (\rho_m u_x^2 + P)}{\partial x} + S_f \,, \tag{4}$$

$$\frac{\partial E}{\partial t} = -\frac{\partial ([E+P] u_x)}{\partial x} + S_h \,. \tag{5}$$

Here, E is the total energy of the flow per unit volume, as described by:

$$E = \rho e + \frac{1}{2}\rho u_x^2 \,, \tag{6}$$

where e is the specific internal energy of the mixture. To capture the physics of internal H_2 flows, Eqs. (4) and (5) include two separate source terms, namely S_f and S_h. The former accounts for losses owing to flow viscosity and its interaction with the wall, whereas the latter caters for a constant heat influx from the pipe wall to the flowing LH_2 stream:

$$S_f = \frac{\rho_m f u_x |u_x|}{2D} \quad , \quad S_h = C \,, \tag{7}$$

where D is the pipe diameter and C is an arbitrary constant heat flux. Note the viscous dissipation term S_f incorporates the mixture density ρ_m, hence extending the functionality of the approach to a homogeneous flow. A friction factor f is calculated locally at every cell using Churchill's formula [82], a computationally-efficient variant

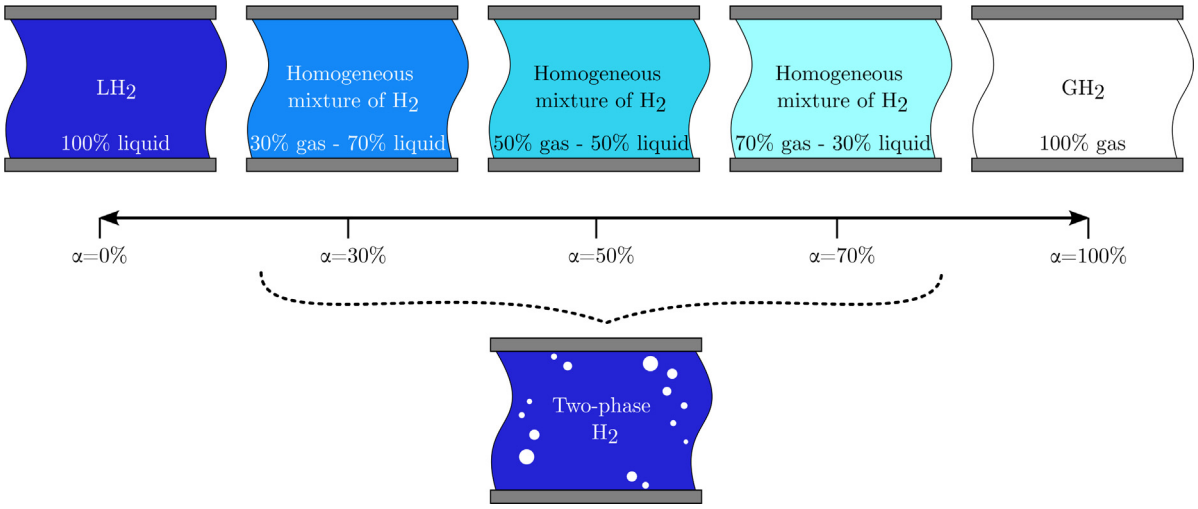

Fig. 2. Conceptual view of a simplified flow representation under a homogeneous equilibrium model.

of the Colebrook equation [83] which does not require of iterative routines:

$$f = 8\left[\left(\frac{8}{\mathrm{Re}}\right)^{12} + \frac{1}{(A+B)^{1.5}}\right]^{1/12}, \tag{8}$$

where A and B are defined as:

$$A = \left\{-2.457\ln\left[\left(\frac{7}{\mathrm{Re}}\right)^{0.9} + \frac{\epsilon}{3.7D}\right]\right\}^{16} \quad ; \quad B = \left(\frac{37,530}{Re}\right)^{16}, \tag{9}$$

where ϵ is the pipe surface roughness. This approach allows for the integration of unsteady friction losses in the momentum equation by considering the local Reynolds number of a cell and its change between successive iterations. This formulation addresses the pressure overpredictions reported in ESPSS (see Section 1.2) and enhances the accuracy of the resulting pressure-field predictions by accounting for the higher attenuation of two-phase frictional effects. It is also worth noting that, while the total energy equation should include an additional source term representing frictional losses, this is neglected owing to H_2's low viscosity range $\sim \mathcal{O}(10^{-6}$ to 10^{-5} Pa s). Consequently, emphasis is placed on resolving the momentum equation, where frictional effects are dominant.

2.2. The multiparametric EOS for parahydrogen

To close the system of Eqs. (3)–(5), a multiparametric EoS was selected to relate pressure and density [38,39]. Multiparametric equations of state are mainly expressed in terms of the Helmholtz free energy (A), which is split between an ideal (A°) and a residual (A^r) contribution. The first term accounts for the thermodynamic behaviour of an ideal gas, whereas the latter considers the deviation of a specific substance from this baseline. The total Helmholtz free energy is then expressed as:

$$A(\rho,T) = A^\circ(\rho,T) + A^r(\rho,T)\,. \tag{10}$$

By reformulating the above expression, one can introduce the non-dimensional Helmholtz energy (a) as:

$$a(\delta,\tau) = a^\circ(\delta,\tau) + a^r(\delta,\tau)\,; \tag{11}$$

in which δ and τ are the non-dimensional variants of the density and temperature inputs in Eq. (10):

$$\delta = \frac{\rho}{\rho_c} \quad ; \quad \tau = \frac{T_c}{T}\,. \tag{12}$$

Here, ρ_c and T_c denote the density and temperature at the critical point. Expressing an EoS in terms of the Helmholtz free energy is done for convenience, as all other thermodynamic properties can be obtained from its derivatives. For instance, the pressure (P) and specific internal energy (e) can be determined using the following relations:

$$P = \rho RT\left[1 + \delta\left(\frac{\partial a^r}{\partial\delta}\right)_\tau\right] \quad ; \quad \frac{e}{RT} = \tau\left[\left(\frac{\partial a^\circ}{\partial\tau}\right)_\delta + \left(\frac{\partial a^r}{\partial\tau}\right)_\delta\right]. \tag{13}$$

As described in Eqs. (10) and (11), Helmholtz-energy-based EoSs are formulated in terms of density and temperature, which in turn rely on iterative routines to obtain the remaining properties. This can be especially challenging in the neighbourhood of the critical point, where convergence issues may arise. To avoid these potential issues, the multiparametric EoS used in this work is applied through the `CoolProp` framework, an extensively validated thermophysical property library with proven capability to handle critical and near-critical states [84]. It is important to note that CoolProp is based on the same Hemlholtz free energy formulations as NIST REFPROP [85], and comparative plots between the two libraries can be found for a range of fluids, including air [86], nitrogen [87], methane [88], water [89], and P-H_2 [90]. Because multiparametric equations of state are fluid-specific, `Arpad` employs the formulation of Leachman et al. [77] for P-H_2, distinguishing it from the corresponding models for orthohydrogen (O-H_2) and normal hydrogen (N-H_2). Accordingly, the present analysis assumes that hydrogen liquefaction has been carried out using an ortho-to-parahydrogen conversion catalyst [91–93]. Further details on a brief quantitative assessment of the accuracy and performance of the `CoolProp` library can be found in Section 4.7.

3. Application of the Godunov method to two-phase hydrogen flows

This section introduces the application of a Godunov-type finite-volume framework to the simulation of two-phase hydrogen flows. The discussion firstly addresses spatial discretisation, followed then by the solution to the Riemann problem for H_2. Temporal discretisation is subsequently discussed, and the treatment of non-linear source terms follows. The numerical handling of boundary conditions concludes the section.

3.1. Spatial discretisation

Eqs. (3)–(5) are solved explicitly [94] on a regular cylindrical mesh (see Figs. 3 and 4). The homogeneous system (i.e. with no source terms) is expressed in vector notation as follows:

$$\frac{\partial\mathbf{U}}{\partial t} + \frac{\partial\mathbf{F}(\mathbf{U})}{\partial x} = 0\,, \tag{14}$$

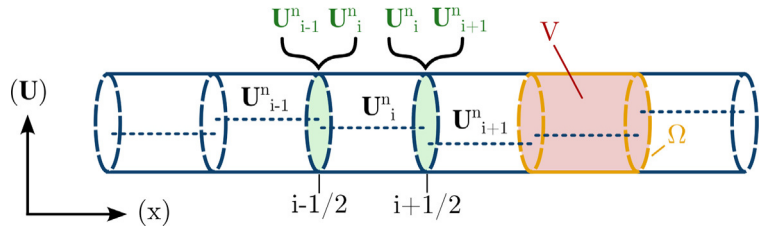

Fig. 3. A depiction of the first-order spatial discretisation, where i denotes the cell index, $i \pm 1/2$ denote the right and left faces of cell i, respectively, and n is the time index.

where the vector of conserved variables $\mathbf{U}$ and the vector of fluxes $\mathbf{F}$ are defined as:

$$\mathbf{U} = \begin{pmatrix} \rho_m \\ \rho_m u_x \\ E \end{pmatrix} \quad ; \quad \mathbf{F}(\mathbf{U}) = \begin{pmatrix} \rho_m u_x \\ \rho_m u_x^2 + p \\ u_x(E+p) \end{pmatrix} . \tag{15}$$

To discretise the above expressions, a finite volume approach is applied by integrating each term over a volume V, bounded by a surface Ω:

$$\frac{\partial}{\partial t}\int_V \mathbf{U} dV + \oint_\Omega \vec{n}\cdot\mathbf{F}(\mathbf{U}) d\Omega = 0 . \tag{16}$$

`Arpad` assumes a first-order interpolation of $\mathbf{U}$ from cell-centroid to face values (see Fig. 3). Consequently, Eq. (16) takes the form:

$$\frac{\partial \mathbf{U}}{\partial t}\int_V dV + \oint_\Omega \vec{n}\cdot\mathbf{F}(\mathbf{U}) d\Omega = 0 , \tag{17}$$

where the second term on the left-hand side (LHS) remains in integral form to account for the fluxes at each cell interface. Discretising Eq. (17) into a set of algebraic equations then yields:

$$\frac{\partial \mathbf{U}}{\partial t} V + \sum_{face=0}^{faces} \vec{n}\cdot\mathbf{F}(\mathbf{U})_{face}\, \Omega_{face} = 0 . \tag{18}$$

Since 1-D meshes are constrained to spatial variations in one direction (i.e. x-axis), there are only two faces (i.e. $faces = 2$) where the surface integral is applied, thus reducing the previous expression to:

$$\frac{\partial \mathbf{U}}{\partial t} V + \left(\mathbf{F}(\mathbf{U})_{i+1/2} - \mathbf{F}(\mathbf{U})_{i-1/2}\right) \Omega_{face} = 0 , \tag{19}$$

where, $\mathbf{F}(\mathbf{U})_{i+1/2}$ and $\mathbf{F}(\mathbf{U})_{i-1/2}$ are the fluxes at the right and left interfaces of cell i. For a cylindrical control volume, of diameter D and length Δx, the cell volume and face area are given by $V = \pi D^2 \Delta x/4$ and $\Omega_{face} = \pi D^2/4$, respectively. Substituting these expressions into the previous equation and dividing through by V leads to:

$$\frac{\partial \mathbf{U}}{\partial t} + \frac{1}{\Delta x}\left(\mathbf{F}(\mathbf{U})_{i+1/2} - \mathbf{F}(\mathbf{U})_{i-1/2}\right) = 0. \tag{20}$$

Because properties are only known at the cell centres, the flux at each face must be reconstructed through interpolation. The present work applies a piece-wise constant reconstruction, and it therefore assumes a face value equal to that of the centroid (i.e. $\phi_{i-1/2} = \phi_i = \phi_{i+1/2}$). Consequently, this leads to the well-known Riemann problem at every cell interface (e.g. $i \pm \frac{1}{2}$), for there are now two candidate states — one from cell i ($\mathrm{U}^{\mathrm{L}}_{i+1/2}$) and another from cell $i+1$ ($\mathrm{U}^{\mathrm{R}}_{i+1-1/2}$) — to evaluate the flux $\mathbf{F}(\mathbf{U})_{i+1/2}$.

3.2. Solution of the Riemann problem for hydrogen

The Godunov method [70] is implemented using the Rusanov approximate Riemann solver [95]. Within this framework, the method computes a single interfacial flux $\tilde{\mathbf{F}}(\mathbf{U})_{i+1/2}$ by resolving the discontinuity between the adjacent cell states, $\mathbf{U}^n_i$ and $\mathbf{U}^n_{i+1}$, at the interface $i+1/2$ (see Fig. 3). These states are relabelled as $\mathbf{U}^L_{i+1/2}$ and $\mathbf{U}^R_{i+1/2}$ to denote the left and right values in the local Riemann problem. The resulting interfacial flux, obtained from the approximate solution of this problem, is then expressed as:

$$\tilde{\mathbf{F}}(\mathbf{U})_{i+1/2} = \frac{1}{2}\left[\mathbf{F}(\mathbf{U}^L_{i+1/2}) + \mathbf{F}(\mathbf{U}^R_{i+1/2})\right] - \lambda\left(\mathbf{U}^R_{i+1/2} - \mathbf{U}^L_{i+1/2}\right) , \tag{21}$$

where λ is an estimation for the fastest local wave speed described by:

$$\lambda = \max(|u_{xL}| + c_L, |u_{x_R}| + c_R) , \tag{22}$$

with c being the speed of sound derived from `CoolProp`'s [84] transport property models. Likewise, the same set of steps apply to the left interface of cell i, (i.e. the face at $i-1/2$), yielding the intercell flux approximation for $\tilde{\mathbf{F}}(\mathbf{U})_{i-1/2}$. As a final step, both approximate fluxes are substituted into Eq. (20) to give:

$$\frac{\partial \mathbf{U}}{\partial t} + \frac{1}{\Delta x}\left(\tilde{\mathbf{F}}(\mathbf{U})_{i+1/2} - \tilde{\mathbf{F}}(\mathbf{U})_{i-1/2}\right) = 0 , \tag{23}$$

completing the spatial discretisation of Eqs. (3)–(5).

3.3. Temporal discretisation

Time integration is achieved through the forward Euler method, which is a first-order upwind explicit scheme [96]. Starting from a Taylor series expansion:

$$\mathbf{U}(t+\Delta t) = \mathbf{U}(t) + \frac{\partial \mathbf{U}}{\partial t}\Delta t + \mathcal{O}(\Delta t^2) . \tag{24}$$

A first-order approximation of the time derivative is then obtained by

$$\frac{\partial \mathbf{U}}{\partial t} = \frac{\mathbf{U}(t+\Delta t) - \mathbf{U}(t)}{\Delta t} + \mathcal{O}(\Delta t) . \tag{25}$$

Applying time superscripts (i.e. n for t, $n+1$ for $t+\Delta t$) we now get:

$$\frac{\partial \mathbf{U}}{\partial t} \approx \frac{\mathbf{U}^{n+1} - \mathbf{U}^n}{\Delta t} , \tag{26}$$

which is later inserted into Eq. (23) to yield the fully discretised set of equations in space and time:

$$\mathbf{U}^{n+1}_i = \mathbf{U}^n_i - \frac{\Delta t}{\Delta x}\left(\tilde{\mathbf{F}}(\mathbf{U})^n_{i+1/2} - \tilde{\mathbf{F}}(\mathbf{U})^n_{i-1/2}\right) . \tag{27}$$

Note that both flux vectors $\tilde{\mathbf{F}}(\mathbf{U}_{i+1/2})$, $\tilde{\mathbf{F}}(\mathbf{U}_{i-1/2})$ are evaluated at time level n, therefore adjusting to an explicit time discretisation scheme with a single unknown at the LHS.

3.4. Implementation of the non-linear source terms

Sections 3.1–3.3 have so far considered only the homogeneous form (i.e., without source terms) of the governing equations. In practice, however, Eqs. (3)–(5) constitute an inhomogeneous system, obtained by introducing the source vector $\mathbf{S}(\mathbf{U})$ on the right-hand side (RHS) of Eq. (14). The system is therefore rewritten as

$$\frac{\partial \mathbf{U}}{\partial t} + \frac{\partial \mathbf{F}(\mathbf{U})}{\partial x} = \mathbf{S}(\mathbf{U}) , \tag{28}$$

where the source term vector $\mathbf{S}(\mathbf{U})$ is defined as

$$\mathbf{S}(\mathbf{U}) = \begin{pmatrix} 0 \\ \frac{f\rho_m |u_x| u_x}{2D} \\ C \end{pmatrix} . \tag{29}$$

To extend the framework beyond simple advection, an operator-splitting scheme is employed following [97]. This approach

decomposes the inhomogeneous system into two subproblems: advection and source terms. The advection component is treated by solving the homogeneous counterpart of the system (see Eq. (14)), whereas the source component assumes no spatial variations in the fluxes and reduces the problem to a system of ordinary differential equations (ODEs). The ODE system is solved after the advection step, enabling an exact treatment of the source term.

3.5. Specification of boundary conditions

Boundary conditions (BCs) were implemented through combinations of Dirichlet and Neumann formulations, following [98]. Prescribed values were directly applied to mesh boundary nodes, with each derived condition (inlet, outlet, wall, etc.) detailed in this section.

3.5.1. Numerical treatment of subsonic inflow and outflow boundaries

Subsonic inflow boundaries were imposed by prescribing density and the normal velocity component (Dirichlet), while static pressure was extrapolated from the domain (Neumann), thereby emulating an inlet mass flow. Outflow boundaries prescribed static pressure (Dirichlet), with the remaining variables extrapolated from interior nodes (Neumann).

3.5.2. Sonic outlet boundary under non-linear conditions

A non-linear treatment is proposed for sonic outflow boundaries within the context of a FVM framework through the implementation of root-finding methods. Such boundaries are relevant in the context of full-bore rupture of pipelines containing pressurised gases, an extensively studied scenario by health and safety agencies [99–108]. After rupture, the following gas decompression requires accurate prediction of the transient mass flow discharge. A time-dependent boundary treatment is therefore necessary, as prescribing a standard supersonic outlet (i.e. Dirichlet conditions for all flow variables) would impose non-physical constant discharge rates.

To address this, a dedicated boundary subroutine is implemented to solve the local Riemann problem at the rupture location by determining the thermodynamic state at the pipe outlet (see Fig. 4). The required information is available at the last computational cell centroid (denoted by subscript I) and from the ambient conditions (subscript atm), allowing the outlet state (subscript out) to be inferred through a set of simplifying assumptions. First, isenthalpic behaviour is considered, in alignment with standard treatments of choked flow at pipe exits during full-bore ruptures [99,108], and justified by the relatively small variations in flow properties expected over a distance of $\Delta x/2$. Second, irreversibilities over this length scale are neglected, leading to an isentropic approximation (see Eq. (30)). These assumptions enable the outlet pressure (P_{out}) to be determined via a bounded nonlinear root-finding procedure, such as the bisection method [109], which identifies an intermediate pressure between the upstream centroid value (P_I) and the ambient pressure (P_{atm}). The root-finding algorithm is applied to the enthalpy balance in Eq. (30) to obtain a representative outlet state, from which the remaining thermodynamic properties are evaluated using the pressure–entropy input pair to query the `CoolProp` database [84]. Accordingly, the enthalpy balance between centroid and boundary is expressed as

$$f(h_I, h_{out}) = \left[h_I(P_I, s_I) + \tfrac{1}{2}u_{xI}^2\right] - \left[h_{out}(P_{out}, s_{out}) + \tfrac{1}{2}c^2\right] = 0, \quad \text{where} \quad s_I = s_{out}\,. \tag{30}$$

Here, the subscript I denotes the flow properties at the last cell centroid, and the outlet velocity is set to the local speed of sound c, to emulate the choked-flow conditions at the exit during full-bore ruptures.

3.5.3. Numerical treatment of non-penetrating boundary conditions (wall)

Wall boundaries are enforced by prescribing a Dirichlet condition on the normal velocity, set explicitly to zero, while all other flow variables are assigned Neumann conditions through zero-gradient extrapolation from the interior. Since the present study is restricted to 1-D meshes, wall boundaries here correspond to closed pipe ends.

4. Results and discussion

To verify the implementation of the suggested FVM approach, this section presents seven sets of numerical tests conducted on pipes with circular cross-sections. *Case 1* examines the classical shock tube problem to validate `Arpad`'s discontinuity-capturing capability. *Case 2* considers a Fanno flow, used to assess the implementation of steady friction models. *Case 3* studies a Rayleigh flow, highlighting the correct addition of constant heat transfer. *Case 4* investigates the combined effects of Fanno and Rayleigh flows (i.e. combined heat transfer and steady friction effects). *Case 5* addresses pipe decompression following a full-bore rupture, providing verification of the unsteady friction model described by Eqs. (8) and (9). *Case 6* revisits a well-studied two-phase water shock tube problem to verify the solver's capability with phase-change phenomena [110–112]. Finally, *Case 7* presents a novel two-phase shock tube test using P-H_2 as the working fluid to demonstrate the method's applicability to cryogenic LH_2 flows. It should be noted that, while *Cases 1–6* do not involve LH_2 as the working fluid and are not descriptive of the expected conditions in LH_2 fuel systems, their purpose is to be used for methodological verification, following the guidelines of Roache [113]. As a result, their discussion simply addresses the robustness of the proposed Godunov approach. Consequently, is through this verification process that a solid foundation is laid for its subsequent application to LH_2 flows. The numerical setup for each case is summarised in Tables 1–3, listing the geometry, discretisation, source terms and initial parameters. Boundary conditions are also detailed in Table 4 for the sake of completeness.

Transient simulation results additionally account for the effect of different Riemann solvers in the solution. Riemann solvers are a key component of Godunov-type schemes, as they are responsible for computing the numerical fluxes that will update the conserved variables in the domain. Riemann solvers are what make the Godunov approach particularly suited for handling flow discontinuities, and their effects are explored by applying the Rusanov [95], HLL [114] and HLLC [114] variants. The inclusion of HLL and HLLC solvers is motivated by their ability to counterbalance the inherently diffusive nature of first-order piecewise reconstructions, especially in the presence of contact discontinuities. The main difference among these is their treatment of the wave structure in the solution of the Riemann problem, which in turn affects the amount of numerical diffusion introduced in the solution. A Rusanov solver is the most diffusive, as it solves the Riemann problem by considering only one characteristic field (i.e. the fastest wavespeed). The HLL solver mitigates numerical diffusion by considering two characteristic fields (i.e. the fastest and slowest wavespeeds), but this still renders the solution incomplete. An HLLC approach, is the least diffusive as it considers all three characteristic fields (i.e. the fastest, slowest and contact wavespeeds), thus providing a more complete solution, and the sharpest definition of the flow fields [115]. Simulations involving static flow solutions (i.e. *Cases 2–4*), however, are solved only using the Rusanov solver, as the absence of flow discontinuities in these cases renders the use of more complex solvers unnecessary. For *Cases 1–4*, which admit analytical solutions, each study concludes with the evaluation of relative L_2-norm errors for the primitive variables. The choice to report this error only for the mentioned cases reflects both the availability of closed-form reference solutions and the consistent use of the Rusanov solver. The relative L_2-norm error for a generic field

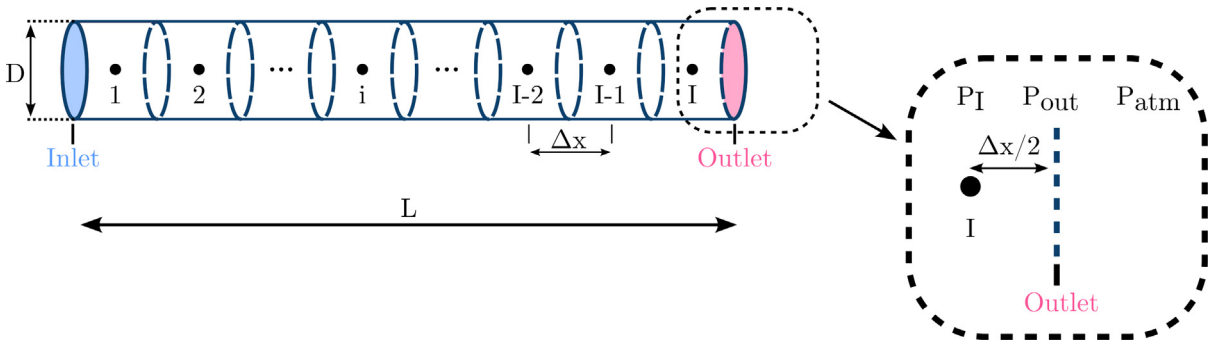

Fig. 4. A view of the discretised pipe domain, indicating the location and bounds of the non-linear sonic outlet.

Table 1
Numerical and geometric parameters for each test case.

Case	Fluid	L [m]	D [m]	Cells	Courant No.	Final time [s]
(1) Sod's shock tube [116]	Air	1.00×10^{0}	1.128	2000	0.5	2.00×10^{-1}
(2) Fanno flow [117,118]	N_2	8.15×10^{1}	0.152	1000	0.9	2.50×10^{1}
(3) Rayleigh flow [117,118]	N_2	8.15×10^{1}	0.152	1000	0.9	2.50×10^{1}
(4) Fanno–Rayleigh [117]	N_2	8.15×10^{1}	0.152	1000	0.9	3.05×10^{1}
5) Pipe rupture [108]	CH_4	8.00×10^{3}	0.870	4000	0.9	3.25×10^{2}
(6) Two-phase water shock-tube [112]	H_2O	1.00×10^{2}	1.128	2000	0.8	8.10×10^{-2}
(7) Two-phase p-H_2 shock-tube	P-H_2	1.00×10^{2}	1.128	2000	0.8	6.10×10^{-2}

Table 2
Initial conditions for Cases 1, 6 and 7.

Case	Initial conditions					
	ρ_L [kg/m^3]	u_{xL} [m/s]	P_L [bar]	ρ_R [kg/m^3]	u_{xR} [m/s]	P_R [bar]
(1) Sod's shock tube	1.000	0.0	1.0	0.125	0.0	0.1
(6) Two-phase water shock tube	552.882	0.0	150.0	371.799	0.0	100.0
(7) Two-phase p-H_2 shock tube	46.115	0.0	10.0	33.463	0.0	5.0

Table 3
Initial conditions for Cases 2, 3, 4, and 5.

Case	Initial conditions					
	ρ [kg/m^3]	u_x [m/s]	P [bar]	$\dot{Q}$ [W]	$C=\frac{\dot{Q}}{Cells}$ [W]	f
(2) Fanno flow	3.876	0.0	3.45	0	0	0.002
(3) Rayleigh flow	3.876	0.0	3.45	2202	2.202	0.000
(4) Fanno–Rayleigh	3.876	0.0	3.45	585	0.585	0.002
(5) Pipe rupture	78.322	0.0	100.00	0	0	$f(Re)$

variable ζ is defined as

$$\|\zeta\|_{L_2}=\frac{\left(\sum_{i=1}^{I}\left(\zeta_i-\zeta_i^{\mathrm{ref}}\right)^2\right)^{1/2}}{\left(\sum_{i=1}^{I}\left(\zeta_i^{\mathrm{ref}}\right)^2\right)^{1/2}}, \tag{31}$$

where ζ_i^{ref} denotes the analytical solution evaluated at the cell centroids and I is the total number of computational cells.

4.1. Case 1: Sod's shock tube

Verification begins with the classical Sod shock tube test, a standard benchmark for assessing numerical performance in the presence of flow discontinuities [116]. The domain consists of two regions of air initially at rest ($u_x=0$), separated by a diaphragm at the centre ($x=0$). Air is modelled as an ideal gas through the relation $P=\rho(\gamma-1)e$. At $t=0$, the diaphragm is removed, initiating a Riemann problem whose solution features a shock wave, an expansion wave, and a contact discontinuity. For the initial conditions listed in Table 2, a semi-analytical reference solution is available via the method of characteristics [119].

Before drawing conclusions from any numerical results, however, a grid convergence index (GCI) analysis was performed to quantify the discretisation error associated with spatial grid resolution. The present work followed the methodology described by Celik et al. [120], using the density field values at $x=0.26$, $x=0.69$ and $x=0.85$ at $t=0.2$ s as the quantity of interest ψ. Said points were selected because they correspond to the corners at the peak of the rarefaction wave, contact discontinuity and the shock wave respectively, representing those points in which discontinuities in the solution occur. Three uniform

Table 4
Boundary conditions for all test cases; density (kg/m^3), velocity (m/s), pressure (bar).

	Boundary values			Notes
(1) Sod shock-tube				
Inlet	$\partial\rho/\partial x=0$	$\partial u_x/\partial x=0$	$\partial P/\partial x=0$	Neumann
Outlet	$\partial\rho/\partial x=0$	$\partial u_x/\partial x=0$	$\partial P/\partial x=0$	Neumann
(2) Fanno flow				
Inlet	$\rho=3.876$	$u_x=176.46$	$\partial P/\partial x=0$	Mass flow inlet
Outlet	$\partial\rho/\partial x=0$	$\partial u_x/\partial x=0$	$P=1.62$	Static pressure outlet
(3) Rayleigh flow				
Inlet	$\rho=3.876$	$u_x=162.36$	$\partial P/\partial x=0$	Mass flow inlet
Outlet	$\partial\rho/\partial x=0$	$\partial u_x/\partial x=0$	$P=1.86$	Static pressure outlet
(4) Fanno–Rayleigh flow				
Inlet	$\rho=3.876$	$u_x=158.83$	$\partial P/\partial x=0$	Mass flow inlet
Outlet	$\partial\rho/\partial x=0$	$\partial u_x/\partial x=0$	$P=1.55$	Static pressure outlet
(5) Pipe rupture				
Inlet	$\partial\rho/\partial x=0$	$u_x=0$	$\partial P/\partial x=0$	Wall BCs
Outlet	$\rho(t)$	$u_x(t)$	$P(t)$	Sonic outlet (see Section 3.5.2)
(6) Two-phase water shock tube				
Inlet	$\partial\rho/\partial x=0$	$\partial u_x/\partial x=0$	$\partial P/\partial x=0$	Neumann
Outlet	$\partial\rho/\partial x=0$	$\partial u_x/\partial x=0$	$\partial P/\partial x=0$	Neumann
(7) Two-phase P-H_2 shock tube				
Inlet	$\partial\rho/\partial x=0$	$\partial u_x/\partial x=0$	$\partial P/\partial x=0$	Neumann
Outlet	$\partial\rho/\partial x=0$	$\partial u_x/\partial x=0$	$\partial P/\partial x=0$	Neumann

Table 5
Grid convergence study over 3 grids for Sod's shock tube using the Rusanov, HLL and HLLC Riemann solvers. ψ represents density at $x = 0.69$ m and $\psi_{extrapolated}$ its extrapolated value. r the refinement ratio between two successive grids. GCI is the grid convergence index in percent and its asymptotic value is provided by $GCI_{asymptotic}$, where a value close to unity indicates a grid independent solution. The order achieved in the simulation is given by p.

	ψ	$Cells$	r	GCI	$GCI_{asymptotic}$	p	$\psi_{extrapolated}$
Rusanov							
Grid 1	3.521e−01	4000	2.0	21.77%			
Grid 2	3.47e−01	2000	2.0	24.03%	1.015	0.12	4.13e−01
Grid 3	3.41e−01	1000	–	–			
HLL							
Grid 1	3.498e−01	4000	2.0	0.17%			
Grid 2	3.52e−01	2000	2.0	0.79%	0.995	2.27	3.49e−01
Grid 3	3.43e−01	1000	–	–			
HLLC							
Grid 1	3.528e−01	4000	2.0	0.66%			
Grid 2	3.56e−01	2000	2.0	1.85%	0.990	1.49	3.51e−01
Grid 3	3.47e−01	1000	–	–			

Table 6
L_2-norm relative errors for the Sod shock tube problem computed using the Rusanov Riemann solver.

$\|\rho\|_{L_2}$	$\|u_x\|_{L_2}$	$\|P\|_{L_2}$	$\|e\|_{L_2}$
1.64%	0.99%	2.00%	2.75%

grids with 1000, 2000 and 4000 cells were considered, corresponding to a coarse, medium and fine resolution, respectively. Table 5 shows the results for the x-location showing the highest discretisation error, (i.e. the contact discontinuity at $x = 0.69$ m). The results achieved indicate, to no surprise, the less dissipative behaviour of the HLL and HLLC solvers, judging by their limited change across different grids. Although 4000-cell grids provide the lowest GCI values across every solver, grids with 2000 cells achieved low enough GCI values (i.e. with the HLL and HLLC solvers) to provide a sufficiently sharp solution of the contact discontinuity. Therefore, the 2000-cell grid was selected for subsequent analysis.

As shown in Fig. 5, the present scheme accurately reproduces the expected wave structure and captures sharp gradients in the flow variables. Although the agreement is generally good, minor discrepancies can be observed near the sharp bends and corners of the solution, where the numerical profiles tend to smooth discontinuities and round the corners caused by steep gradients. This behaviour is characteristic of first-order accurate schemes, which inherently introduce numerical diffusion. The effect is further enhanced by the use of the Rusanov Riemann solver, known to be more dissipative than alternative approximate solvers such as HLL or HLLC [114]. Similar trends are expected in the subsequent test cases for analogous reasons. Table 6 gathers the $L2$-norm relative errors obtained with the Rusanov Riemann solver for the flow variables reported in Fig. 5.

4.2. Case 2: Fanno flow

The second test looked at validating flow viscosity effects through the description of a Fanno flow [118]. This refers to an adiabatic flow through a constant constant-area duct where friction is the main source of irreversibility (i.e. entropy generation). The problem is set up using gaseous nitrogen (N_2) as the working fluid, and modelled as an ideal gas $P = \rho(\gamma - 1)e$. Viscous effects are captured via a constant Darcy–Weisbach friction factor [121], which induces flow acceleration along the pipe length when it departs from subsonic conditions. A defining characteristic is the existence of a finite duct length at which the flow becomes sonic. This critical length serves as the theoretical upper bound for the computational domain in Fanno flow simulations, and it is equally the case for the current test. A comprehensive description is provided in [117]. It should be noted that the solution of interest corresponds to the final steady state (for which an analytical solution is available) despite the inherently transient nature of the problem.

Table 7
Grid convergence study over 3 grids for a Fanno flow using the Rusanov solver. ψ represents the integral of static pressure along the pipe length and $\psi_{extrapolated}$ its extrapolated value. $Cells$ is the number of grid elements, r the refinement ratio between two successive grids. GCI is the grid convergence index in percent and its asymptotic value is provided by $GCI_{asymptotic}$, where a value close to unity indicates a grid independent solution. The order achieved in the simulation is given by p.

	ψ	$Cells$	r	GCI	$GCI_{asymptotic}$	p	$\psi_{extrapolated}$
Grid 1	2.284e+07	2000	2.0	1.13%			
Grid 2	2.27e+07	1000	2.0	1.73%	1.005	0.60	2.31e+07
Grid 3	2.26e+07	500	–	–			

Table 8
L_2-norm relative errors for the Fanno flow problem computed using the Rusanov Riemann solver.

$\|T/T^*\|_{L_2}$	$\|P/P^*\|_{L_2}$
0.74%	2.33%

A GCI analysis was also conducted for the Fanno flow case following the procedure outlined in the previous section; however, only results obtained with the Rusanov solver were considered. This choice is motivated by the fact that Fanno flow solutions do not involve contact discontinuities, and the flow ultimately reaches a steady state, for which negligible differences are expected among Riemann solvers. The same rationale will inform the compressible flow cases described in Sections 4.3–4.5. As *Cases 2–4* involve inherently steady solutions, additional tables showing the normalised L-2 norm residuals for the temperature and pressure fields are provided to demonstrate solution convergence (see Table 13). The computed residuals are as specified below:

$$\mathcal{R}_\phi = \frac{\left\|\phi^{n+1} - \phi^n\right\|_2}{\left\|\phi^1 - \phi^0\right\|_2}, \tag{32}$$

where ϕ is the field variable of interest (i.e. temperature or pressure), and n is the iteration number. Note that the normalising factor corresponds to initial residual after the first iteration. The final time reported in Table 1 for these cases hence corresponds to the time at which the solution was considered to be well within the asymptotic convergence range, as indicated by the residuals.

For such a case, mesh densities of 500, 1000 and 2000 cells were studied, and the quantity of interest ψ corresponded to the static pressure integral along the pipe length after reaching a steady solution at $t = 25.0$ s. Eq. (33) describes the quantity of interest, and the resulting values are summarised in Table 7. Judging by the small difference between the fine and medium grid resolutions (i.e. only of 0.60%), the 1000-cell grid was considered sufficiently accurate for verification, thus results achieved with a medium grid are presented. Fig. 6 illustrates the good agreement between the analytical and numerical solution, verifying the implementation of steady friction models in `Arpad`. The L_2-norm relative errors for the flow variables shown in Fig. 6, computed using the Rusanov solver, are listed in Table 8.

$$\psi = \int_0^L P(x)\,dx\,. \tag{33}$$

4.3. Case 3: Rayleigh flow

Unlike the case in Section 4.2, where viscous dissipation drives the change in flow properties, Rayleigh flows are governed by heat transfer between the fluid and its surroundings [118]. It is through the addition of heat, therefore, that the flow is accelerated (and entropy increased) along the pipe– ultimately leading to sonic conditions at the outlet. Rayleigh flows assume an inviscid, steady flow in a constant-area duct,

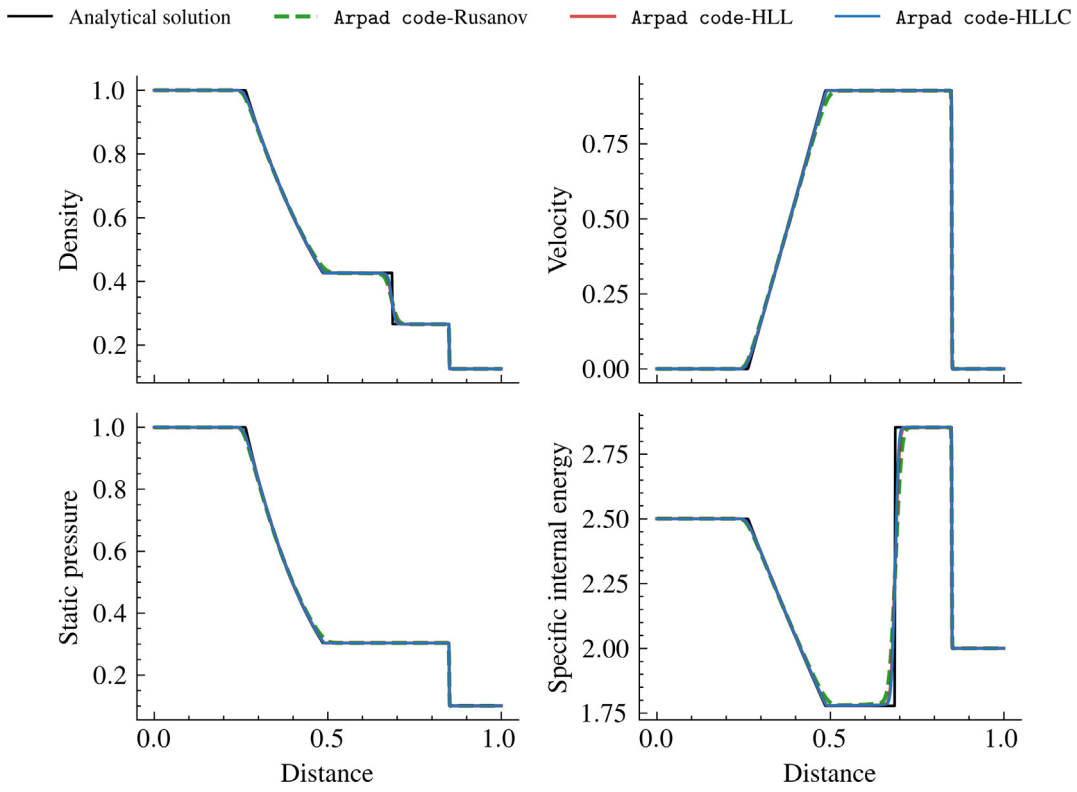

Fig. 5. Sod shock tube fields obtained for an ideal gas.

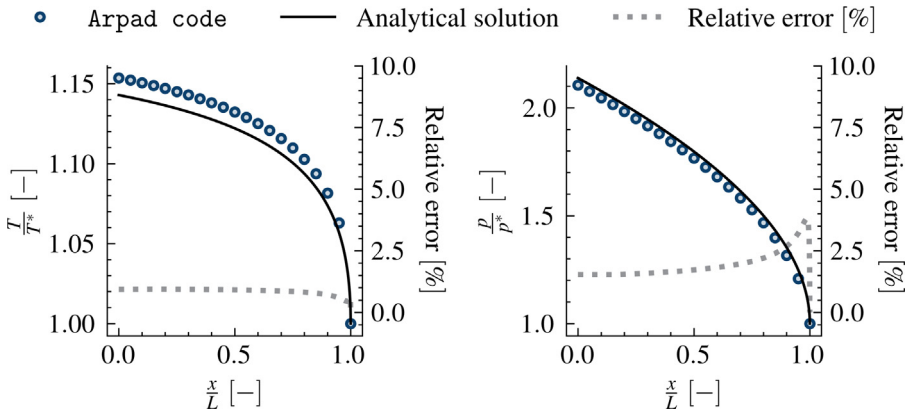

Fig. 6. Fanno flow temperature and pressure fields.

thus providing a suitable test case to isolate the effects of a constant and uniform energy exchange.

Similarly, a GCI analysis was conducted as described in Section 4.2. The main difference lied in the quantity of interest ψ, which now corresponded to the integral of the temperature field along the pipe length after reaching a steady state solution at $t = 25.0$ s.

$$\psi = \int_0^L T(x)\, dx\,. \tag{34}$$

The working fluid is again ideal gaseous N_2, and the flow exhibits a maximum duct length at which heat addition chokes the pipe. This characteristic length sets the effective limit of the computational domain, as detailed in [117]. As it was the case for the Fanno flow, the 1000-cell grid was considered sufficiently accurate for verification considering the small difference between the fine and medium grid resolutions shown in Table 9 (i.e. only of 0.31%). Fig. 7 illustrates the scheme's ability to reproduce the effects of uniform heat addition. The close agreement between analytical and numerical solutions verifies the correct treatment of thermal energy exchange. The computed relative L_2-norm errors for the variables depicted in Fig. 7 are summarised in Table 10 for the Rusanov solver

Table 9
Grid convergence study over 3 grids for a Rayleigh flow using the Rusanov solver. ψ represents the integral of the static temperature field along the pipe length and $\psi_{extrapolated}$ its extrapolated value. $Cells$ is the number of grid elements, r the refinement ratio between two successive grids. GCI is the grid convergence index in percent and its asymptotic value is provided by $GCI_{asymptotic}$, where a value close to unity indicates a grid independent solution. The order achieved in the simulation is given by p.

	ψ	$Cells$	r	GCI	$GCI_{asymptotic}$	p	$\psi_{extrapolated}$
Grid 1	3.038e+04	2000	2.0	0.61%			
Grid 2	3.03e+04	1000	2.0	0.92%	1.003	0.61	3.05e+04
Grid 3	3.02e+04	500	–	–			

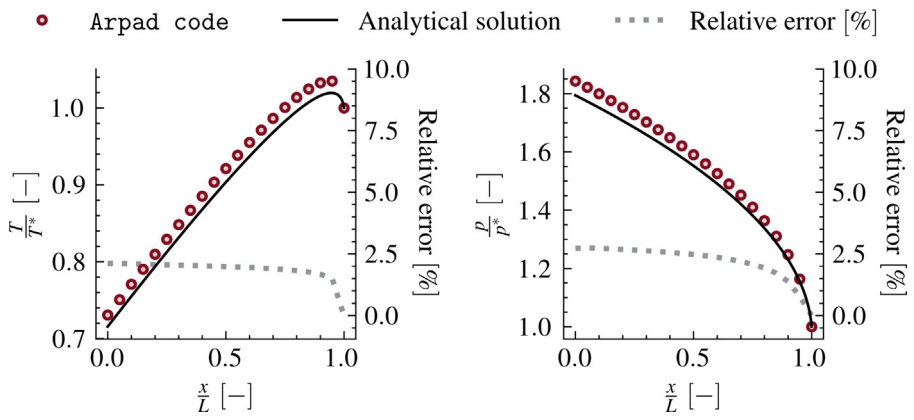

Fig. 7. Rayleigh flow temperature and pressure fields.

Table 10
L_2-norm relative errors for the Rayleigh flow problem computed using the Rusanov Riemann solver.

$\|T/T^*\|_{L_2}$	$\|P/P^*\|_{L_2}$
1.90%	2.42%

Table 11
Grid convergence study over 3 grids for a Fanno–Rayleigh flow using the Rusanov solver. ψ represents the integral of the static temperature field along the pipe length and $\psi_{extrapolated}$ its extrapolated value. $Cells$ is the number of grid elements, r the refinement ratio between two successive grids. GCI is the grid convergence index in percent and its asymptotic value is provided by $GCI_{asymptotic}$, where a value close to unity indicates a grid independent solution. The order achieved in the simulation is given by p.

	ψ	$Cells$	r	GCI	$GCI_{asymptotic}$	p	$\psi_{extrapolated}$
Grid 1	2.566e+04	2000	2.0	0.01%			
Grid 2	2.57e+04	1000	2.0	0.01%	1.000	0.94	2.57e+04
Grid 3	2.57e+04	500	–	–			

Table 12
L_2-norm relative errors for the Fanno–Rayleigh flow problem computed using the Rusanov Riemann solver.

$\|T/T^*\|_{L_2}$	$\|P/P^*\|_{L_2}$
0.07%	4.1%

4.4. Case 4: Fanno-Rayleigh flow

To complement the assessments in Sections 4.2 and 4.3, a combined case was considered to capture the simultaneous effects of friction and heat transfer within a single setup. In this case, both friction and heat addition are the source of irreversibilities accelerating the fluid and leading to choked conditions at the pipe outlet. The test involves subsonic flow of gaseous N_2, modelled as an ideal gas, subject to a constant Darcy–Weisbach friction factor and uniform heat addition [117]. Unlike the individual Fanno and Rayleigh flows, no tabulated solutions are available for this combined case, and the analytical treatment is limited to the Mach number distribution. Nevertheless, pressure and temperature profiles can be obtained by solving the compressible flow equations as an initial value problem.

Following an analogous approach as in the Fanno and Rayleigh cases, a GCI analysis was performed using the integral of the temperature field along the pipe length (see Eq. (34)) after reaching a steady state solution at $t = 30.5$ s (see Table 11). Fig. 8 presents the results, which demonstrate the friction and heat transfer terms reproduce the expected trends when these are combined. Using the Rusanov solver, the relative L_2-norm errors for the flow variables reported in Fig. 8 are compiled in Table 12.

4.5. Case 5: Full-bore rupture of a pipe

While the preceding cases in Sections 4.2 and 4.4 considered a constant friction factor verified through steady flow fields, the current test addresses the verification of the unsteady friction terms discussed in Section 2.1 through an unsteady solution. This is obtained through the transient analysis of a full-bore rupture in a pressure-liquefied gas pipeline. Following a rupture, choked flow conditions are immediately reached at the rupture point, where the flow is dominated by unsteady viscous dissipation. This behaviour, among other effects, leads to a characteristic mass flow discharge following a decreasing asymptotic curve [107,108]. This section hence evaluates the decompression of a pressurised methane (CH_4) pipeline, allowing for friction factor variations (in space and time), that are used to verify unsteady friction losses. Unlike the cases discussed previously, this scenario involves gaseous CH_4 modelled with the multiparametric EoS of Setzmann and Wagner [122] included in the `CoolProp` [84] database.

The GCI analysis conducted in this case used the time integral of the exit mass flow rate throughout the whole event as the quantity of interest ψ (see Eq. (35)). Three uniform grids with 1000, 2000 and 4000 cells were considered, with results being summarised in Table 14. In this case, the 4000-cell grid was selected for subsequent analysis, as it provided a solution with a GCI below 10%.

$$\psi = \int_0^{t_{End}} \dot{m}_{exit}(t)\, dt\,, \tag{35}$$

As full-bore rupture events lack closed-form analytical solutions for the full set of flow fields governed by the conservation laws, verification is performed against established industry codes used in quantitative risk assessment. Examples include `PolyPiRRaM` (HSE)[2] and `PHAST` (DNV GL), both of which focus on predicting mass flow discharge during decompression of pressurised pipelines [107,108,123]. Both `PolyPiRRaM` [107,108] and `PHAST` [123] rely on analytical sub-models to solve the quasi-steady compressible pipe flow equations. In the present configuration, the models are applied without inflow boundary conditions, assuming discharge through a single open end. Within this framework, `PHAST` distinguishes between choked and unchoked two-phase outflow conditions, whereas `PolyPiRRaM` exploits the relative insensitivity of the momentum equation to boundary conditions in the pipe. Finite-volume formulations of the problem have also been proposed in the literature, for instance by Shargatov et al. [106]. Despite having a slight overestimation of the mass flow compared to `PolyPiRRaM` [107,108], and underestimating the value

[2] Health and Safety Executive, United Kingdom.

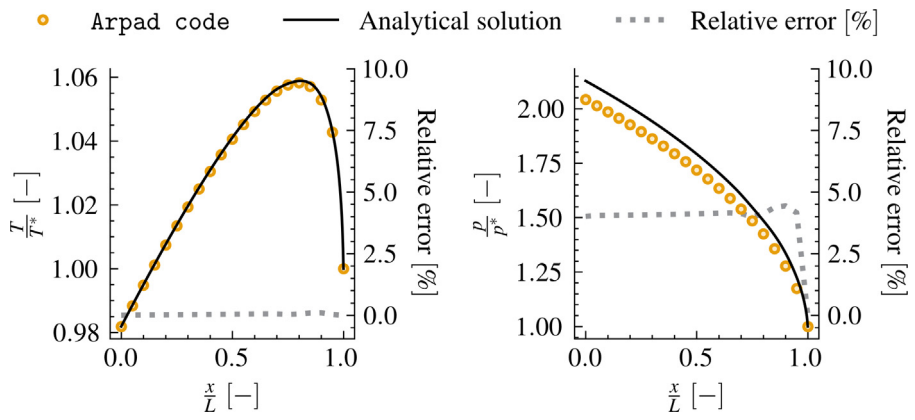

Fig. 8. Fanno–Rayleigh flow pressure and temperature fields.

Table 13
Summary of normalised temperature and pressure residuals (R_T, R_P) for the Fanno, Rayleigh and Fanno–Rayleigh flows using the Rusanov solver. Values are reported at selected iterations and as the window-averaged residual over the last 100 iterations, $\langle R_\phi \rangle_{\text{last 100}}$.

Iteration	Fanno flow		Rayleigh flow		Fanno–Rayleigh flow	
	R_T	R_P	R_T	R_P	R_T	R_P
1	1.00×10^{0}	1.00×10^{0}	1.00×10^{0}	1.00×10^{0}	1.00×10^{0}	1.00×10^{0}
100	5.04×10^{-2}	1.88×10^{-2}	3.67×10^{-2}	1.78×10^{-2}	8.58×10^{-3}	3.68×10^{-3}
1000	2.61×10^{-11}	6.48×10^{-12}	3.93×10^{-12}	2.86×10^{-12}	2.90×10^{-14}	8.18×10^{-15}
$\langle R_\phi \rangle_{\text{last 100}}$	6.34×10^{-15}	2.99×10^{-15}	8.14×10^{-15}	2.95×10^{-15}	3.38×10^{-14}	7.25×10^{-15}

Table 14
Grid convergence study over 3 grids for a pipe decompression flow using the Rusanov solver. ψ represents the time integral of the exit mass flow rate throughout the event, and $\psi_{extrapolated}$ its extrapolated value. $Cells$ is the number of grid elements, r the refinement ratio between two successive grids. GCI is the grid convergence index in percent and its asymptotic value is provided by $GCI_{asymptotic}$, where a value close to unity indicates a grid independent solution. The order achieved in the simulation is given by p.

	ψ	$Cells$	r	GCI	$GCI_{asymptotic}$	p	$\psi_{extrapolated}$
Grid 1	3.153e+05	4000	2.0	9.17%			
Grid 2	3.10e+05	2000	2.0	11.55%	1.018	0.31	3.38e+05
Grid 3	3.03e+05	1000	–	–			

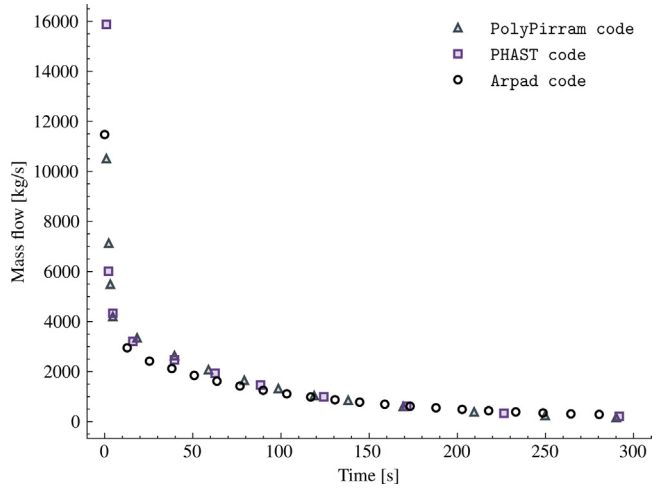

Fig. 9. Methane pipeline decompression exit mass flow rate.
Source: Reproduced from [108] with additional results from the present study.

from PHAST [123] in the initial instants, the results in Fig. 9 demonstrate the suitability of the unsteady friction models implemented in Arpad.

4.6. Case 6: Two-phase water shock tube

To assess Arpad's ability to capture phase-change phenomena and predict wave speeds in two-phase flows, an extension of the classical shock tube problem is considered. The setup consists of a tube filled with water at two distinct saturated states, separated by a diaphragm at $x = 0$. The left state corresponds to a liquid with a vapour volume fraction of 10%, while the right state corresponds to a liquid with a volume fraction of 50%. At $t = 0$, the diaphragm is removed, generating a pressure imbalance that drives shock and rarefaction waves, as well as contact discontinuities driven by condensation and evaporation effects. The acoustic properties of the mixture were computed using Wood's speed of sound model [124,125]:

$$\frac{1}{\rho_m c_m^2} = \frac{\alpha}{\rho_{gas} c_{gas}^2} + \frac{(1-\alpha)}{\rho_{liq} c_{liq}^2}, \tag{36}$$

while wave speeds were estimated following the approach of Batten et al. [126]. Note that the model is extended to the HEM framework using the mixture density ρ_m and speed of sound c_m in the Riemann solver. On this occasion the GCI analysis was performed using the density at $x = 52.0$ m (i.e. the peak value of the boiling front). Three uniform grids with 500, 1000 and 2000 cells were considered for the three Riemann solvers discussed in Section 4.1. Table 15 summarises the achieved discretisation errors. Since the 2000-element mesh provided a significant reduction in the GCI values across all Riemann solvers, this grid was selected for further analysis. Arpad results for different Riemann solvers using the fine grid were then compared against the reference solution from Daude and Galon [112] (see Fig. 10), who studied the same configuration and verified their approach against the RELAP7 [127] code for nuclear safety applications. Note that the zoomed-in views in Fig. 10 are focused on the boiling and condensation fronts of the contact discontinuity, where the differences between Riemann solvers and the reference solution are more pronounced. The present case, at the same time, serves to validate the CoolProp [84] thermophysical database for two-phase flows, since Daude and Galon [112] used the steam-water property tables from the National Bureau of Standards [128] to generate the reference solution.

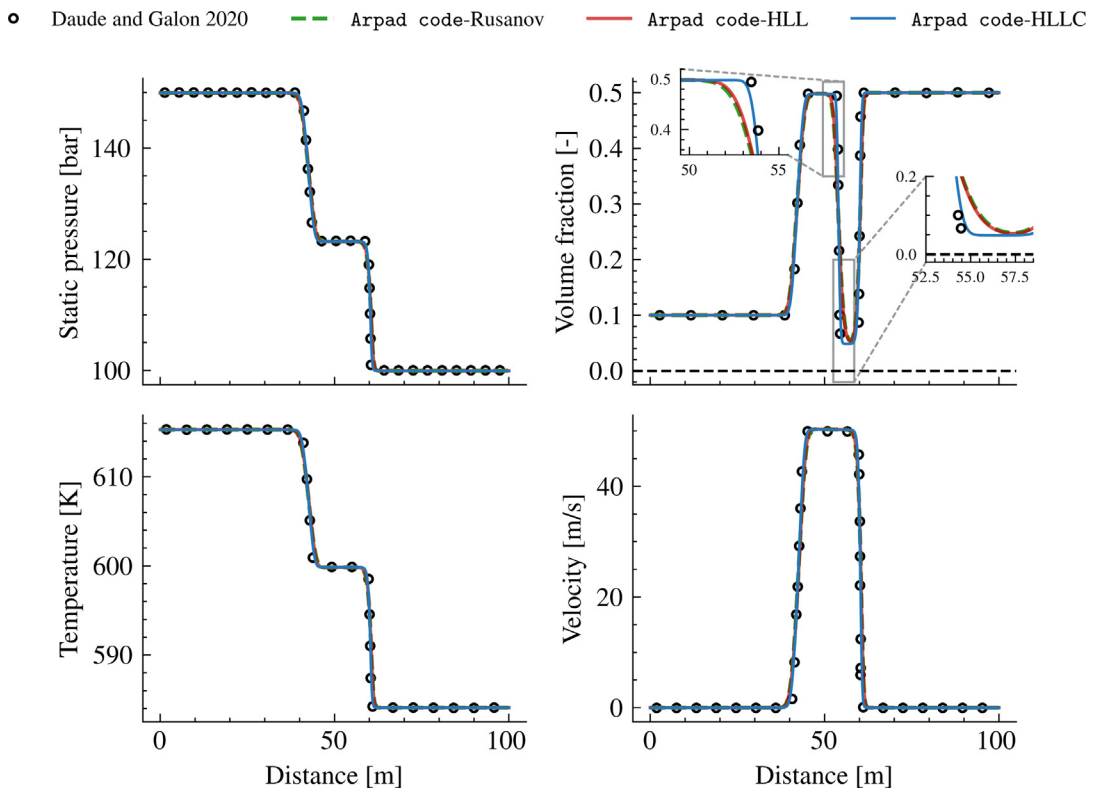

Fig. 10. Two-phase water shock tube fields. Comparison against Daude and Galon [112].

Table 15
Grid convergence study over 3 grids for the two-phase water shock tube problem using the Rusanov, HLL and HLLC Riemann solvers. ψ represents volume fraction at $x = 56.1$ m and $\psi_{extrapolated}$ its extrapolated value. r the refinement ratio between two successive grids. GCI is the grid convergence index in percent and its asymptotic value is provided by $GCI_{asymptotic}$, where a value close to unity indicates a grid independent solution. The order achieved in the simulation is given by p.

	ψ	Cells	r	GCI	$GCI_{asymptotic}$	p	$\psi_{extrapolated}$
Rusanov							
Grid 1	4.801e−01	2000	2.0	43.21%			
Grid 2	4.49e−01	1000	2.0	54.99%	1.070	0.25	6.46e−01
Grid 3	4.11e−01	500	–	–			
HLL							
Grid 1	4.850e−01	2000	2.0	25.56%			
Grid 2	4.56e−01	1000	2.0	35.09%	1.063	0.37	5.84e−01
Grid 3	4.19e−01	500	–	–			
HLLC							
Grid 1	4.981e−01	2000	2.0	0.01%			
Grid 2	4.98e−01	1000	2.0	0.07%	0.999	3.61	4.98e−01
Grid 3	4.95e−01	500	–	–			

4.7. Case 7: Two-phase parahydrogen shock tube

As a final test case, the two-phase shock tube problem is revisited using P-H_2 as the working fluid. The setup follows the same configuration as in Section 4.6, with the tube initially divided in two saturated states by a diaphragm at $x = 0$. The left state corresponds to a liquid with a vapour volume fraction of 10%, while the right state corresponds to a liquid with a vapour fraction of 50%. At $t = 0$, removal of the diaphragm generates a pressure imbalance, producing wave patterns qualitatively similar to those observed in Section 4.6. This case is intended to demonstrate `Arpad`'s ability to model two-phase flows involving LH_2, as this is relevant for assessing transient events in cryogenic management systems. The speed of sound and wave speeds are evaluated using the same methodology as in Section 4.6, but with the thermophysical properties of P-H_2.

Mesh independence was evaluated using the same grid layout for the Riemann solvers specified in the previous section (see Table 16). Similar to the water case, the quantity of interest ψ was defined as the volume fraction at the peak of the boiling front ($x = 50.5$ m). This choice over a point in the trough (i.e. the valley at the condensation front), was motivated by the fact that, for the finest grid and the HLLC solver, the condensation trough reached the pure-liquid limit ($\alpha = 0$), thereby complicating the GCI analysis. The boiling peak, by contrast, remained well within the two-phase regime across all grid resolutions and Riemann solvers, while avoiding numerical issues associated with phase-change boundaries. As in the previous case, the 2000-element mesh was selected for further analysis based on the significant reduction in GCI values across all Riemann solvers.

Among the Riemann solvers considered, HLLC yielded the lowest GCI values, reflecting its superior capability to resolve two-phase contact discontinuities (see Fig. 11). Further evidence of this can be observed in Fig. 12, where a first-order spatial discretisation combined with an HLLC solver, yields similar levels of numerical diffusion as a second-order discretisation with a Rusanov solver and the minmod limiter [129,130] (i.e. assuming the same settings described in Table 1). Note that a second-order approximation, reveals spurious oscillations when implemented in the present framework, (see the static pressure field in Fig. 12), hence breaking the monotonicity of the solution as expected from Godunov's order barrier theorem [70,131]. Unlike the water-based configuration in Section 4.6, no reference solution has been reported in the literature for this P-H_2 shock-tube setup; consequently, results are presented without direct quantitative comparison. Nevertheless, the observed wave structures are consistent with the expected physical behaviour, which might be useful as a reference for verification purposes of two-phase P-H_2 flows. It is also noted that the influence of the chosen Riemann solver becomes most pronounced in the vicinity of the sharp phase-change front separating the liquid and

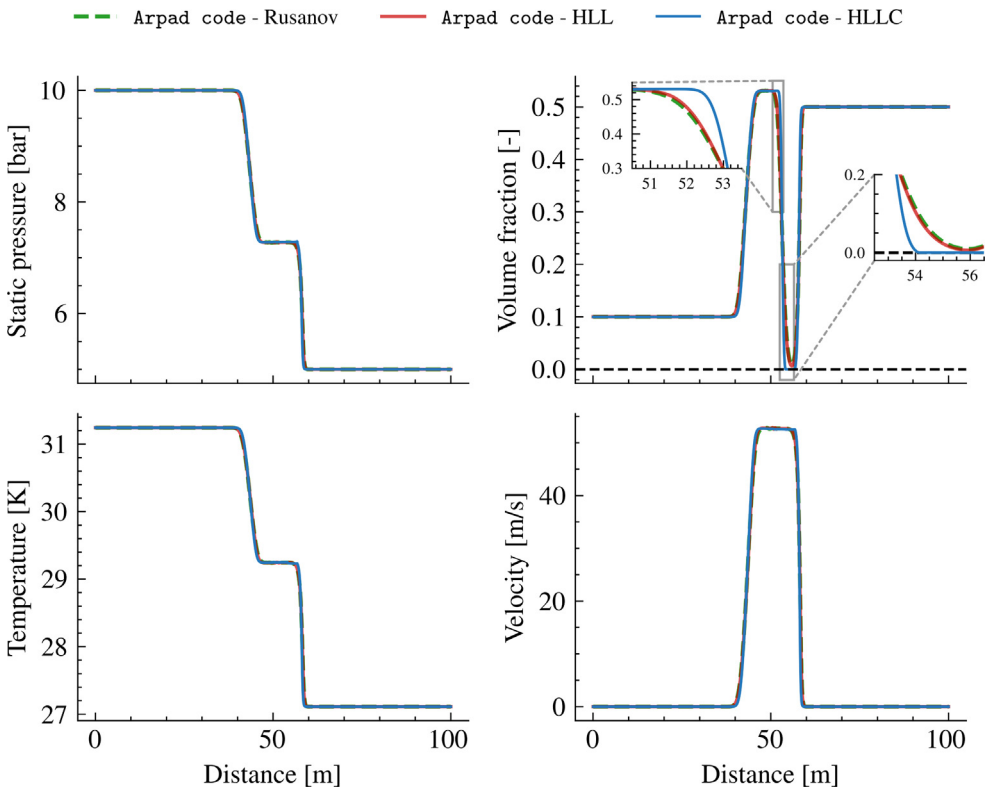

Fig. 11. Two-phase parahydrogen shock tube fields computed with `Arpad`.

Table 16
Grid convergence study over 3 grids for the two-phase P-H_2 shock tube problem using the Rusanov, HLL and HLLC Riemann solvers. ψ represents volume fraction at $x = 46.4$ m and $\psi_{extrapolated}$ its extrapolated value. r the refinement ratio between two successive grids. GCI is the grid convergence index in percent and its asymptotic value is provided by $GCI_{asymptotic}$, where a value close to unity indicates a grid independent solution. The order achieved in the simulation is given by p.

	ψ	Cells	r	GCI	$GCI_{asymptotic}$	p	$\psi_{extrapolated}$
Rusanov							
Grid 1	5.294e−01	2000	2.0	2.47%			
Grid 2	5.16e−01	1000	2.0	5.74%	1.026	1.18	5.40e−01
Grid 3	4.86e−01	500	–	–			
HLL							
Grid 1	5.310e−01	2000	2.0	1.49%			
Grid 2	5.21e−01	1000	2.0	3.93%	1.019	1.37	5.37e−01
Grid 3	4.95e−01	500	–	–			
HLLC							
Grid 1	5.302e−01	2000	2.0	0.13%			
Grid 2	5.31e−01	1000	2.0	0.05%	0.119	1.54	5.30e−01
Grid 3	5.32e−01	500	–	–			

two-phase regions, where the solution approaches the limit $\alpha \to 0$. In this regime, numerical sensitivity increases, underscoring the superior performance of the HLLC Riemann-solver when modelling two-phase flows near the subcooled boundary of the phase diagram.

While the test cases presented above demonstrate the capability of the model to capture physical aspects related to cryogenic flow management, certain limitations of the present framework should nevertheless be acknowledged. First, it should be noted that the present work relies on the homogeneous equilibrium assumption, which restricts its applicability to flows in which the phases remain well mixed (e.g. high Reynolds internal flows with uniform heat transfer). Consequently, the approach may become inadequate when simulating stratified flows (often observed in horizontal pipelines), where the phases are clearly separated. In addition, while a constant heat transfer term was considered and verified in Section 4.3, this simplification does not capture the spatial and temporal variations of heat transfer that usually arise in cryogenic pipelines.

Before concluding this section, a brief implementation remark is provided to clarify numerical choices that are essential for reproducing the results discussed. For the present case, since `Arpad` relies on `CoolProp` [84] as a backend for thermodynamic property evaluation, specific measures were adopted to ensure a robust and accurate treatment of the two-phase region. In particular, all calls to the `CoolProp` [84] high-level interface were enforced using temperature (T) and density (ρ) as input variables. This choice was motivated both by a significant reduction in computational cost and by the need to avoid flash calculations, which may introduce convergence issues across successive solver iterations. When phase-equilibrium (flash) calculations are triggered within `CoolProp` [84], thermodynamic properties are obtained through iterative root-finding procedures. In the present implementation, these calculations rely on the Brent method [132] to determine the equilibrium state. While generally robust, such routines can occasionally yield numerical outliers, particularly on finely discretised meshes where small perturbations in the input variables may amplify the numerical output (see Fig. 13).

This behaviour can lead to convergence difficulties in the flow solver, as illustrated in Fig. 13. In this case, despite the thermodynamic state remaining well within the two-phase region and at pressure levels of approximately 7 bar, minor variations at the decimal level resulted in non-physical pressure values (see Table 17). These anomalies are attributed to the sensitivity of Brent-based flash calculations under tightly clustered thermodynamic states, rather than to deficiencies in the underlying physical model. For this reason, enforcing thermodynamic evaluations based on T and ρ was adopted, as this approach avoids flash calculations altogether by directly evaluating the Helmholtz energy derivatives (see Section 2.2), thereby ensuring smoother property fields and improved numerical robustness.

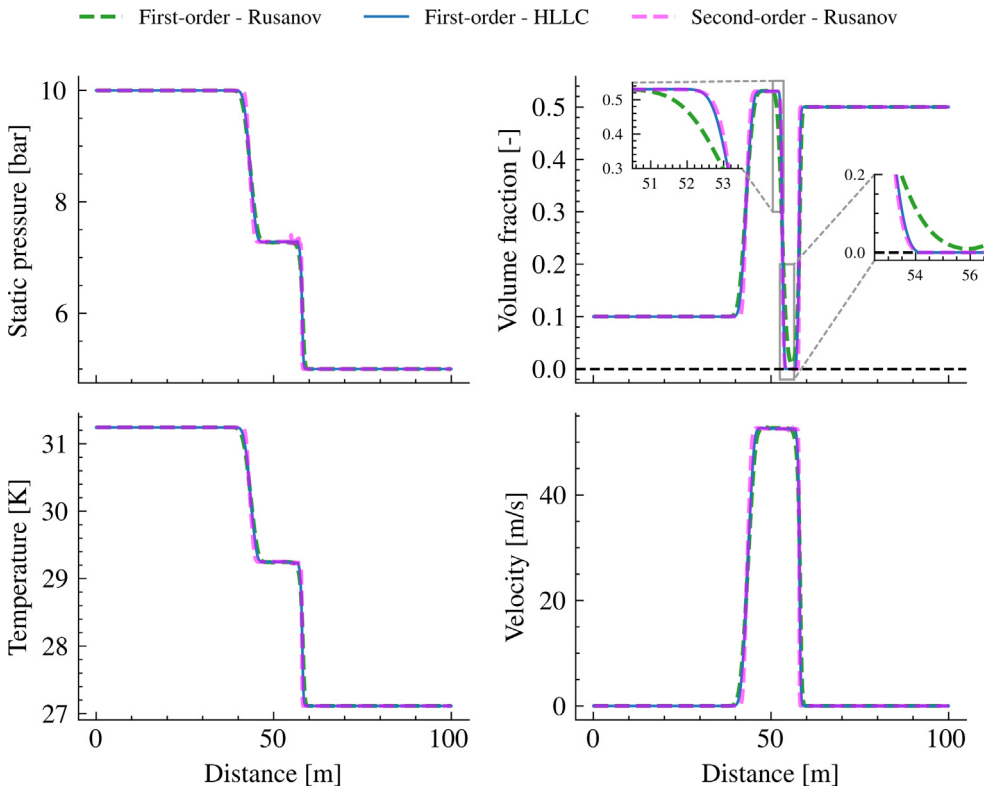

Fig. 12. Two-phase parahydrogen shock tube fields computed with `Arpad` using first- and second-order spatial discretisations.

Table 17
Thermodynamic states used to illustrate the divergence behaviour in Fig. 13.

Point	Query variables		Output variable
	ρ [kg/m^3]	e [J/kg]	P [bar]
A	31.4463	154 566.4607	7.32
B	31.4464	154 566.5482	113.43
C	31.4466	154 566.6356	7.32

A second implementation measure was introduced to ensure consistency in single-phase regions. `CoolProp` [84] does not directly provide the vapour volume fraction α, but instead returns the vapour mass fraction Q. The two quantities are related through

$$\alpha = \frac{Q/\rho_{\text{gas}}}{Q/\rho_{\text{gas}} + (1-Q)/\rho_{\text{liq}}} \,. \tag{37}$$

While this relation is well-defined in the two-phase regime, `CoolProp` [84] may return non-physical values of Q when the thermodynamic state lies well within the single-phase regions (i.e. subcooled liquid or superheated gas). Such values can, in turn, yield unphysical volume fractions. To prevent this behaviour, the mass fraction Q was explicitly set to unity or zero when the local density exceeded or fell below the saturation limits, respectively. This enforcement avoids spurious values (e.g. $Q = -1$) in single-phase states and ensures physically consistent volume-fraction fields. Accordingly, a lightweight subroutine was implemented to identify the local phase regime following each `CoolProp` [84] call and apply the appropriate constraint.

Since thermodynamic data of parahydrogen P-H_2 is sporadic in the literature, therefore, the NIST chemistry database [133] has been employed to benchmark the accuracy of the `CoolProp` [84] library. To quantify the performance of the `CoolProp` library, its output values are obtained through the resolution of Eqs. (11)–(13) and compared with the NIST reference data [133]. Densities along the liquid and gaseous saturation curves including the critical point are summarised in Table 18. The selected values allow for comparing both phases and bound the thermodynamic states observed in Figs. 11 and 12. The resulting values show small relative errors of the Helmholtz EoS implemented in `CoolProp` (see Table 18). The case of maximum deviation remains within a small range $\sim \mathcal{O}(10^{-2})$ due to the fact that it relies on empirical data to model the non-ideal behaviour of the fluid (see residual component in Eq. (11)). This emphasises the suitability of the `CoolProp` library [84] for simulating two-phase P-H_2 flows, as it is able to represent thermodynamic behaviour of the fluid flow across its entire phase envelope within a range of small relative errors.

5. Conclusions

This work presents a finite-volume formulation based on a Godunov-type approach for the simulation of two-phase hydrogen flows in pipelines, motivated by the need to capture transient flow phenomena relevant to cryogenic fuel system architectures. The method employs a homogeneous equilibrium model coupled with the thermophysical property library `CoolProp` [84] to evaluate the thermodynamic and transport properties of parahydrogen. To describe the physics of internal flows, wall effects were represented through an unsteady friction model for the momentum equation, whereas heat transfer between the pipe wall and the fluid was captured through a constant source term in the energy equation.

Method performance was assessed through seven benchmark cases targeting isolated physical aspects involved in cryogenic pipe flows. A single-phase shock tube with air confirmed the capability of the scheme to resolve shock waves, rarefaction waves, and contact discontinuities, with excellent agreement against the exact solution to the Sod shock-tube problem [116]. The inclusion of steady wall friction and heat transfer was assessed through the simulation of Fanno, Rayleigh, and combined Fanno–Rayleigh flows [118] using gaseous N_2 as the working fluid, also showing good agreement with analytical predictions. To evaluate the proposed unsteady two-phase friction models, a pipe rupture benchmark was considered, requiring a non-linear treatment for a sonic outlet boundary condition. Results were then compared

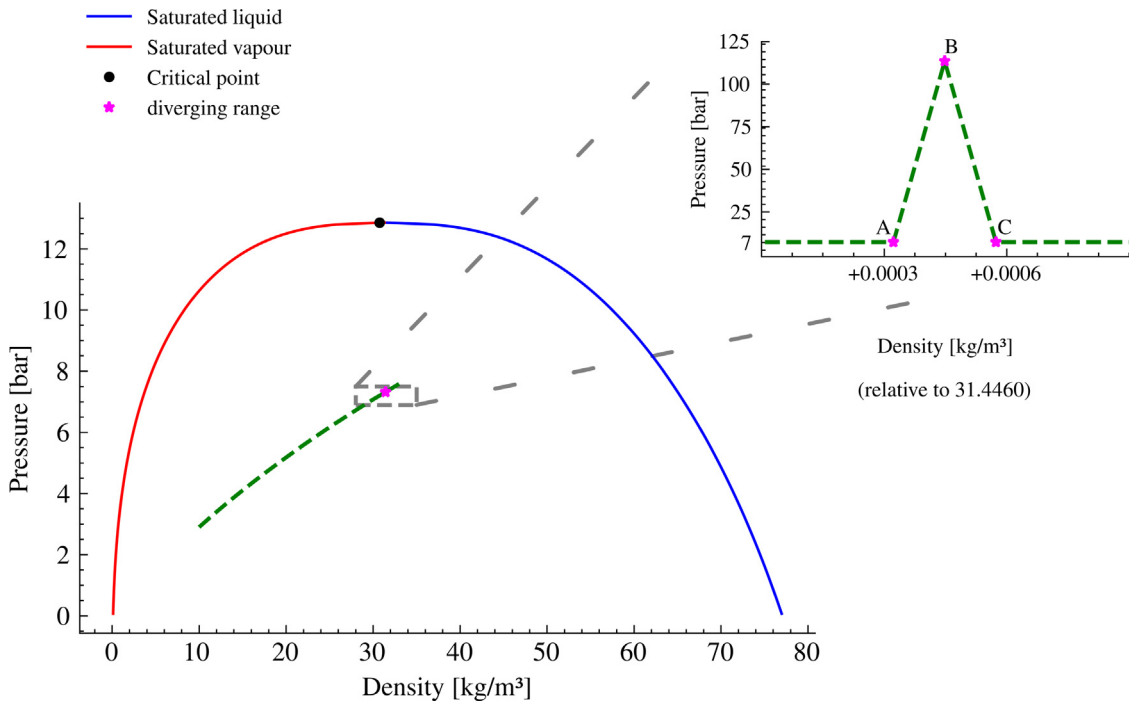

Fig. 13. Parahydrogen divergence error using CoolProp [84].

Table 18
Comparison of density predictions for saturated liquid and gas states against NIST reference data [133] for parahydrogen. The HEOS superscript denotes the density predictions from the Helmholtz EoS implemented in `CoolProp` [84]. The relative error (δ) for each phase is calculated as $\delta = \left(|\rho^{\text{NIST}} - \rho^{\text{HEOS}}|/\rho^{\text{NIST}}\right) \cdot 100$.

Parahydrogen ($P\text{-}H_2$)							
Saturation states							
T [K]	P [bar]	ρ_{liq}^{NIST} [kg/m^3]	ρ_{liq}^{HEOS} [kg/m^3]	δ_{liq} [%]	ρ_{gas}^{NIST} [kg/m^3]	ρ_{gas}^{HEOS} [kg/m^3]	δ_{gas} [%]
18.0	0.48	73.252	73.251	1.33×10^{-4}	0.688	0.688	5.37×10^{-4}
25.0	3.29	64.485	64.484	3.44×10^{-4}	4.018	4.018	7.48×10^{-4}
32.0	11.20	45.901	45.900	1.34×10^{-5}	17.492	17.492	2.61×10^{-3}
Critical state							
T [K]	P [bar]	ρ^{NIST} [kg/m^3]		ρ^{HEOS} [kg/m^3]		δ [%]	
32.94	12.86	31.323		31.300		7.61×10^{-2}	

against those from risk analysis tools `PolyPiRRaM` [107,108] and `PHAST` [123], demonstrating good predictive accuracy for the discharge rate of high-pressure methane pipelines. For the benchmark cases admitting analytical solutions, the relative L_2-norm errors reported in Tables 6, 8, 10, and 12 indicate a consistent and suitable level of accuracy across all conserved variables. When averaged over these cases, the relative L_2-norm error obtained with the Rusanov Riemann solver was 1.90%, demonstrating good agreement with well-established compressible-flow benchmarks.

Finally, a two-phase shock tube problem was revisited using water and parahydrogen as working fluids to test the solver's capability in capturing phase-change phenomena. The water case was verified against the reference solution of Daude and Galon [112], confirming the correct resolution of condensation and boiling waves. The parahydrogen shock tube problem, reported here for the first time, exhibited wave structures consistent with those observed in water, thereby extending the applicability of the approach to cryogenic fluids of practical relevance. The reported results present a first dataset tailored for two-phase parahydrogen flows which may be used as a reference for future modelling efforts. Finally, this case draws attention to the influence of Riemann solver choice in thermodynamic regimes close to the subcooled liquid limit, where HLLC outperforms noticeably the HLL and Rusanov solvers. As the vapour volume fraction diminishes towards the zero-limit, solver-dependent variations in the predicted volume fraction become more pronounced. This observation indicates that solver selection may play a non-trivial role in the numerical modelling of cryogenic hydrogen systems, specifically in scenarios where accurate volume fraction predictions are critical.

While the present framework demonstrates the capability to capture key two-phase flow features, including boiling and condensation fronts, it is subject to certain limitations. In particular, the homogeneous equilibrium assumption restricts its applicability to flows in which the phases remain well mixed, as occurs in high Reynolds-number internal flows with uniform heat transfer. Its use in horizontal pipelines may therefore be limited, since gravity can induce a clear distinction between phases (i.e. stratified flows). In addition, the constant heat transfer term employed in Section 4.3 does not capture the spatial and temporal variations observed in cryogenic pipelines and requires further verification in future work. Another important consideration is that the proposed framework is currently limited to 1-D flows, which considerably simplifies the underlying physics of wall-effects and neglects the influence of geometry and turbulence. The approach, however, can be extended to 2-D and 3-D schemes as a subject of future efforts.

Overall, this work establishes a foundation for the future simulation of LH_2 two-phase transients in cryogenic pipelines. The verified

benchmarks demonstrate that the Godunov framework is capable of capturing the coupled phenomena — shock propagation, heat transfer, frictional losses, and phase change — that govern the flow physics of cryogenic management systems. Consequently, the present study highlights the potential of Godunov-type methods as a basis for future system-level tools in hydrogen infrastructure design. Through improved understanding of these numerical schemes, Godunov-type methods could be further developed to model (at least at a preliminary level) scenarios of practical interest (i.e. engine start-up, tank feeding switch, or ground refuelling). Future developments will focus on providing detailed comparisons with well-established system-level tools, such as GFSSP and ESPSS, using cases representative of cryogenic fuel system scenarios. In addition, the capabilities of Arpad will be extended to incorporate variable heat transfer coefficients and empirical boiling correlations, together with criteria for flow regime transitions. In parallel, further investigations will assess viscous dissipation effects across a broader range of LH_2 pipe flow conditions relevant to fuel system operations.

CRediT authorship contribution statement

Nicolás Capmany: Writing – original draft, Visualization, Validation, Software, Methodology, Investigation, Formal analysis, Data curation, Conceptualization. **László Könözsy:** Writing – review & editing, Validation, Supervision, Resources, Project administration, Investigation, Formal analysis. **Drewan Sanders:** Writing – review & editing, Validation, Supervision, Resources, Project administration, Investigation, Funding acquisition, Formal analysis.

Declaration of competing interest

The authors declare that they have no known competing financial interests or personal relationships that could have appeared to influence the work reported in this paper.

Acknowledgements

The authors gratefully acknowledge the financial support provided by Innovate UK, part of UK Research and Innovation (UKRI), for the UK Aerospace Technology Institute projects: Zero Emissions for Sustainable Transport (ZEST1) and Future Engine Technology for the Control of Hydrogen (FETCH), under grant agreement s No: 103136 and 10065215, respectively.

Special thanks are extended to Dr Theoklis Nikolaidis (Cranfield University) for his invaluable assistance in securing funding. The authors also wish to express their gratitude to Mr Roberto Alegre (AIRBUS), Dr Andrew Newton (HSE), Dr Neys Schreiner (Cranfield University), Dr Tom-Robin Teschner (Cranfield University), and Dr Frédéric Daude (EDF R&D) for their technical expertise and insightful advice throughout the research.

References

[1] Verstraete D. Long range transport aircraft using hydrogen fuel. Int J Hydrog Energy 2013;38:14824–31.
[2] Verstraete D. On the energy efficiency of hydrogen-fuelled transport aircraft. Int J Hydrog Energy 2015;40:7388–94.
[3] Huete J, Pilidis P. Parametric study on tank integration for hydrogen civil aviation propulsion. Int J Hydrog Energy 2021;46:37049–62.
[4] Rompokos P, Rolt A, Nalianda D, Sibilli T, Benson C. Cryogenic fuel storage modelling and optimisation for aircraft applications. In: Volume 6: Ceramics and ceramic composites; coal, biomass, hydrogen, and alternative fuels; microturbines, turbochargers, and small turbomachines. Virtual, Online: American Society of Mechanical Engineers; 2021, http://dx.doi.org/10.1115/gt2021-58595, URL: https://asmedigitalcollection.asme.org/GT/proceedings/GT2021/84997/V006T03A001/1120121.
[5] Stroman RO, Schuette MW, Swider-Lyons K, Rodgers JA, Edwards DJ. Liquid hydrogen fuel system design and demonstration in a small long endurance air vehicle. Int J Hydrog Energy 2014;39:11279–90.
[6] Ebrahimi A, Rolt A, Jafari S, Anton JH. A review on liquid hydrogen fuel systems in aircraft applications for gas turbine engines. Int J Hydrog Energy 2024;91:88–105.
[7] Leachman JW, Wilhelmsen O, Matveev KI. 2 Thermophysical properties. In: Cool fuel: the science and engineering of cryogenic hydrogen. Oxford scholarship online, Oxford: Oxford University Press; 2025, http://dx.doi.org/10.1093/9780198936688.001.0001.
[8] Veres J. A survey of instabilities within centrifugal pumps and concepts for improving the flow range of pumps in rocket engines. NASA Tech. Rep. Server, 1992.
[9] Veres J. Centrifugal and axial pump design and off-design performance prediction. NASA Tech. Rep. Server, 1995.
[10] Veres J, Lavelle T. Mean line pump flow model in rocket engine system simulation. NASA Tech. Rep. Server, 2000.
[11] Boccardi G, Bubbico R, Celata GP, Di Tosto F. Geometry influence on safety valves sizing in two-phase flow. J Loss Prev Process Ind 2008;21(1):66–73.
[12] Schmidt J, Egan S. Case studies of sizing pressure relief valves for two-phase flow. Chem Eng Technol 2009;32(2):263–72.
[13] Kourakos V, Rambaud P, Buchlin J-M, Chabane S. Flowforce in a safety relief valve under incompressible, compressible, and two-phase flow conditions. J Press Vessel Technol 2013;135(1).
[14] Dempster W, Elmayyah W. Two phase discharge flow prediction in safety valves. Int J Press Vessels Pip 2013;110:61–5.
[15] Zeghloul A, Azzi A, Saidj F, Messilem A, Azzopardi BJ. Pressure drop through orifices for single- and two-phase vertically upward flow—Implication for metering. J Fluids Eng 2017;139(3).
[16] Ma Y, Zhang M, Luo H. Numerical and experimental studies of gas–liquid flow and pressure drop in multiphase pump valves. Sci Prog 2020;103(3).
[17] Flynn T. 9 cryogenic equipment and cryogenic systems analysis. In: Cryogenic engineering, revised and expanded. 0 ed. CRC Press; 2004, http://dx.doi.org/10.1201/9780203026991, URL: https://www.taylorfrancis.com/books/9780203026991.
[18] Barron RF, Nellis GF. 7 two-phase heat transfer and pressure drop. In: Cryogenic heat transfer. 2nd ed. Boca Raton: CRC Press, Taylor & Francis Group; 2016, http://dx.doi.org/10.1201/b20225.
[19] Ruspini L, Marcel C, Clausse A. Two-phase flow instabilities: A review. Int J Heat Mass Transfer 2014;71:521–48.
[20] Brennan J, Brentari E, Smith R, Steward W. An experimental report on cooldown of cryogenic transfer lines. Technical Report 9264, Boulder, Colorado: National Bureau of Standards; 1965.
[21] Van Dresar NT. Cryogenic transfer line chilldown. In: AIP conference proceedings. Vol. 710, Anchorage, Alaska (USA): AIP; 2004, p. 308–15. http://dx.doi.org/10.1063/1.1774697, URL: https://pubs.aip.org/aip/acp/article/710/1/308-315/1000404. ISSN: 0094-243X.
[22] Esposito C. Study of cryogenic transient flows. The impact of the fluid thermosensitivity on cavitation (Ph.D. thesis), KU Leuven; 2020, URL: https://kuleuven.limo.libis.be/discovery/fulldisplay?docid=lirias3041084&context=SearchWebhook&vid=32KUL_KUL:Lirias&search_scope=lirias_profile&adaptor=SearchWebhook&tab=LIRIAS&query=any,contains,LIRIAS3041084&offset=0.
[23] Esposito C, Steelant J, Vetrano MR. Impact of cryogenics on cavitation through an orifice: a review. Energies 2021;14. http://dx.doi.org/10.3390/en14248319.
[24] Hu H, Chung JN, Amber SH. An experimental study on flow patterns and heat transfer characteristics during cryogenic chilldown in a vertical pipe. Cryogenics 2012;52(4–6):268–77, Publisher: Elsevier BV.
[25] Jin L, Cho H, Lee C, Jeong S. Experimental research and numerical simulation on cryogenic line chill-down process. Cryogenics 2017.
[26] Hartwig J, Styborski J, McQuillen J, Rame E, Chung J. Liquid hydrogen line chilldown experiments at high Reynolds Numbers. Optimal chilldown methods. Int J Heat Mass Transfer 2019;137:703–13.
[27] Hartwig J, Styborski J, Stiegemeier B, Chung J, Ramé E, McQuillen J. Liquid hydrogen line chilldown experiments at high Reynolds numbers. II. Analysis. Int J Heat Mass Transfer 2020;156:119805.
[28] Siemens Digital Industries Software. Propulsion system simulation. 2025, URL: https://plm.sw.siemens.com/en-US/simcenter/simulation-test/propulsion-system-simulation/. © Siemens 2025.
[29] Siemens Digital Industries Software. Thermo-fluid system simulation. 2025, URL: https://plm.sw.siemens.com/en-US/simcenter/simulation-test/thermo-fluid-system-simulation/. © Siemens 2025.
[30] Borutzky W, editor. Bond graph modelling of engineering systems. New York, NY: Springer New York; 2011, http://dx.doi.org/10.1007/978-1-4419-9368-7.
[31] Falsetti C. From boiling to cryogenics: The role of two-phase flow in sustainable aviation. In: Lecture presented at the workshop on two-phase flow and cryogenic technologies for space and aviation. Belgium: Von Karman Institute for Fluid Dynamics; 2025.
[32] National Aeronautics and Space Administration. Generalized Fluid System Simulation Program (GFSSP). 2025, URL: https://www.nasa.gov/gfssp/.
[33] National Aeronautics and Space Administration. Generalized fluid system simulation program (GFSSP), version 702 (educational version)(MFS-32929-1) | NASA software catalog. NASA Technology Transfer Program; 2025, URL: https://software.nasa.gov/software/MFS-32929-1.

[34] Majumdar A, Ravindran SS. Numerical prediction of conjugate heat transfer in fluid network. J Propuls Power 2011;27:620–30.

[35] Majumdar A, LeClair A, Moore R, Schallhorn P. Generalized fluid system simulation program, version 6.0. 2016, URL: https://www.nasa.gov/gfssp/.

[36] LeClair A, Hartwig JW, Hauser DM, Kassemi M, Diaz-Hyland P, Going T. Modeling cryogenic chilldown of a transfer line with GFSSP. In: 2018 joint propulsion conference. Reston, Virginia: American Institute of Aeronautics and Astronautics; 2018, http://dx.doi.org/10.2514/6.2018-4756.

[37] Runchal A, editor. A finite volume procedure for thermofluid system analysis in a flow network. In: 50 years of CFD in engineering sciences: A commemorative volume in memory of D. Brian Spalding. 1st ed. Singapore: Springer Singapore; 2020, p. 231–68. http://dx.doi.org/10.1007/978-981-15-2670-1, URL: http://link.springer.com/10.1007/978-981-15-2670-1.

[38] Span R. Multiparameter equations of state. Berlin, Heidelberg: Springer Berlin Heidelberg; 2000, http://dx.doi.org/10.1007/978-3-662-04092-8, URL: http://link.springer.com/10.1007/978-3-662-04092-8.

[39] Span R, Wagner W, Lemmon EW, Jacobsen RT. Multiparameter equations of state—recent trends and future challenges. Fluid Phase Equilib 2001;1–20.

[40] Wilhelmsen Ø, Aasen A, Skaugen G, Aursand P, Austegard A, Aursand E, Gjennestad MA, Lund H, Linga G, Hammer M. Thermodynamic modeling with equations of state: Present challenges with established methods. Ind Eng Chem Res 2017.

[41] Nasrifar K. Comparative study of eleven equations of state in predicting the thermodynamic properties of hydrogen. Int J Hydrog Energy 2010;35(8):3802–11.

[42] Miropolski ZL. Heat transfer in film boiling of steam–water mixture in steam generating tubes. Teploenergetika 1963;10(5):49–52.

[43] Rame E, Hartwig JW, McQuillen JB. Flow visualization of liquid hydrogen line chill down tests. In: 52nd aerospace sciences meeting. National Harbor, Maryland: American Institute of Aeronautics and Astronautics; 2014, http://dx.doi.org/10.2514/6.2014-1074, URL: https://arc.aiaa.org/doi/10.2514/6.2014-1074.

[44] Hartwig J, Hu H, Styborski J, Chung JN. Comparison of cryogenic flow boiling in liquid nitrogen and liquid hydrogen chilldown experiments. Int J Heat Mass Transfer 2015;88:662–73.

[45] Shirai Y, Tatsumoto H, Shiotsu M, Hata K, Kobayashi H, Naruo Y, Inatani Y, Kinoshita K. Forced flow boiling heat transfer of liquid hydrogen for superconductor cooling. Cryogenics 2011;51(6):295–9, Publisher: Elsevier BV.

[46] Sakamoto Y, Kobayashi H, Naruo Y, Takesaki Y, Nakajima Y, Furuichi A, Tsujimura H, Kabayama K, Sato T. Investigation of the void fraction–quality correlations for two-phase hydrogen flow based on the capacitive void fraction measurement. Int J Hydrog Energy 2019;44(33):18483–95, Publisher: Elsevier BV.

[47] Sakamoto Y, Kobayashi H, Naruo Y, Takesaki Y, Nakajima Y, Kabayama K, Sato T. Investigation of boiling hydrogen flow characteristics under low-pressure conditions - Flow regime transition characteristics. Int J Hydrog Energy 2021;46(11):8239–52, Publisher: Elsevier BV.

[48] Hartwig J, Darr S, Asencio A. Assessment of existing two phase heat transfer coefficient and critical heat flux correlations for cryogenic flow boiling in pipe quenching experiments. Int J Heat Mass Transfer 2016;93:441–63.

[49] Hartwig J, Darr S, Chung J. Development of two-phase heat transfer correlations for cryogenic transfer line chilldown. In: AIAA SciTech forum. 2017.

[50] Darr SR, Hartwig JW. Two-phase convection heat transfer correlations for liquid hydrogen pipe chilldown. Cryogenics 2020;105:102999.

[51] Darr SR, Hu H, Glikin NG, Hartwig JW, Majumdar AK, Leclair AC, Chung JN. An experimental study on terrestrial cryogenic transfer line chilldown I. Effect of mass flux, equilibrium quality, and inlet subcooling. Int J Heat Mass Transfer 2016;103:1225–42.

[52] Moral J, Perez-Vara R, Steelant J, de Rosa M. ESPSS simulation platform. In: Proceedings of 2010 space propulsion conference. San Sebastian, Spain; 2010, URL: https://www.ecosimpro.com/wp-content/uploads/2015/02/SpacePropulsion2010_ESPSS_simulation_platform.pdf.

[53] Roe PL. Approximate Riemann solvers, parameter vectors, and difference schemes. J Comput Phys 1981;43:357–72.

[54] Liou M-S, Steffen CJ. A new flux splitting scheme. J Comput Phys 1993;107:23–39.

[55] Liou M-S. A sequel to AUSM: AUSM+. J Comput Phys 1996;129:364–82.

[56] Sweby PK. Godunov methods. In: Toro EF, editor. Godunov methods: theory and applications. New York, NY: Springer US; 2001, p. 879–98. http://dx.doi.org/10.1007/978-1-4615-0663-8_85.

[57] Toro EF. Flux vector splitting methods. In: Riemann solvers and numerical methods for fluid dynamics: a practical introduction. Berlin, Heidelberg: Springer Berlin Heidelberg; 2009, http://dx.doi.org/10.1007/b79761, URL: https://link.springer.com/10.1007/b79761.

[58] Raia A. Analysis and optimization of chill-down processes in cryogenic liquid propellant rocket engines (Ph.D. thesis), Torino: Politecnico di Torino; 2023, URL: https://webthesis.biblio.polito.it/26963/.

[59] Lerma M. Multiphase fluid hammer: modeling, experiments and simulations (Ph.D. thesis), Universidade da Coruna; 2013, URL: http://hdl.handle.net/2183/11716.

[60] Porca P, Lema M, Rambaud P, Steelant J. Experimental and numerical multiphase-front fluid hammer. J Propuls Power 2014;30(2):368–76, Publisher: AIAA.

[61] Ponizovskaya-Devine E, Luchinsky DG, Khasin M, Perotti J, Sass J, Brown B. Towards physics based autonomous control of the cryogenic propellant loading system. In: 51st AIAA/SAE/ASEE joint propulsion conference. Reston, Virginia: American Institute of Aeronautics and Astronautics; 2015, http://dx.doi.org/10.2514/6.2015-4215, URL: http://arc.aiaa.org/doi/10.2514/6.2015-4215.

[62] Luchinsky DG, Ponizovskaya-Devine E, Khasin M, Timucin D, Sass J, Perroti J, Brown B. Two-phase flow modeling of the cryogenic propellant loading system. In: 51st AIAA/SAE/ASEE joint propulsion conference. American Institute of Aeronautics and Astronautics Inc, AIAA; 2015, http://dx.doi.org/10.2514/6.2015-4214.

[63] Liles D, Reed W. A semi-implicit method for two-phase fluid dynamics. J Comput Phys 1978;26:390–407.

[64] Patankar S, Spalding D. A calculation procedure for heat, mass and momentum transfer in three-dimensional parabolic flows. Int J Heat Mass Transfer 1972;15:1787–806.

[65] Issa RI. Solution of the implicitly discretised fluid flow equations by operator-splitting. J Comput Phys 1986;62:40–65.

[66] Luchinsky D, Ponizovskaya E, Hafiychuk V, Kashani A, Khasin M. Hierarchy of two-phase flow models for autonomous control of cryogenic loading operation. 2015, http://dx.doi.org/10.1088/1757-899X/101/1/012069.

[67] Luchinsky DG, Khasin M, Timucin D, Sass J, Brown B. Inferential framework for two-fluid model of cryogenic chilldown. Int J Heat Mass Transfer 2017;114:796–808.

[68] Kunniyoor KR, Govind R, Venkateswaran KS, Ghosh P. Liquid hydrogen pipeline chill-down: Mathematical modelling and investigation. Cryogenics 2021;118:103324.

[69] Crank J, Nicolson P. A practical method for numerical evaluation of solutions of partial differential equations of the heat-conduction type. Math Proc Cambridge Philos Soc 1947;43:50–67.

[70] Godunov SK. A difference scheme for numerical computation of discontinuous solutions of equations of fluid dynamics. Math Sb 1959;47(271):271–306.

[71] Einfeldt B. On Godunov-type methods for gas dynamics. SIAM J Numer Anal 1988;25(2):294–318, Publisher: SIAM.

[72] Tallois L, Peluchon S, Gallice G, Villedieu P. Non-conservative Godunov-type schemes: Application to two-phase flows with surface tension using Lagrange-transport splitting strategy. J Comput Phys 2025;532:113958, Publisher: Elsevier BV.

[73] Alias NA, Liang Q, Kesserwani G. A Godunov-type scheme for modelling 1D channel flow with varying width and topography. Comput & Fluids 2011;46(1):88–93.

[74] León AS, Ghidaoui MS, Schmidt AR, García MH. Application of Godunov-type schemes to transient mixed flows. J Hydraul Res 2009;47(2):147–56.

[75] qing Lu Y, Zhou L, Che T-C, jian Xue Z, jie Li Y, ying Hu Y. Godunov-type solutions for gas-liquid two-phase transient flows with gas release effects. J Hydrodyn 2023;35(6):1179–90.

[76] Komissarov SS. A Godunov-type scheme for relativistic magnetohydrodynamics. Mon Not R Astron Soc 1999;303(2):343–66.

[77] Leachman JW, Jacobsen RT, Penoncello SG, Lemmon EW. Fundamental equations of state for parahydrogen, normal hydrogen, and orthohydrogen. J Phys Chem Ref Data 2009;38(3):721–48.

[78] Hartwig J, Styborski J, McQuillen J, Rame E, Chung JN. Liquid hydrogen line chilldown experiments at high Reynolds Numbers. Optimal chilldown methods. Int J Heat Mass Transfer 2019;137:703–13.

[79] Wallis GB. One-dimensional two-phase flow. New York: McGraw-Hill; 1969.

[80] Ishii M, Hibiki T. Chapter 13 drift-flux model. In: Thermo-fluid dynamics of two-phase flow. New York, NY: Springer New York; 2011, p. 393–5. http://dx.doi.org/10.1007/978-1-4419-7985-8, URL: https://link.springer.com/10.1007/978-1-4419-7985-8.

[81] Brennen CE. Fundamentals of multiphase flow. Cambridge [England]; New York: Cambridge University Press; 2005.

[82] Churchill SW. Friction-factor equation spans all fluid-flow regimes. Chem Eng (USA) 1977;84(24):91–2.

[83] Colebrook CF. Turbulent flow in pipes, with particular reference to the transition region between the smooth and rough pipe laws. J Inst Civ Eng 1939;11(4):133–56.

[84] Bell IH, Wronski J, Quoilin S, Lemort V. Pure and pseudo-pure fluid thermophysical property evaluation and the open-source thermophysical property library CoolProp. Ind Eng Chem Res 2014.

[85] Lemmon EW, Bell IH, Huber ML, McLinden MO. NIST standard reference database 23: Reference fluid thermodynamic and transport properties-REFPROP, version 10.0. National Institute of Standards and Technology; 2018, http://dx.doi.org/10.18434/T4/1502528, URL: https://www.nist.gov/srd/refprop.

[86] Bell IH. Air — CoolProp 7.2.0 documentation. 2025, URL: https://coolprop.org/fluid_properties/fluids/Air.html.

[87] Bell IH. Nitrogen — CoolProp 7.2.0 documentation. 2025, URL: https://coolprop.org/fluid_properties/fluids/Nitrogen.html.

[88] Bell IH. Methane — CoolProp 7.2.0 documentation. 2025, URL: https://coolprop.org/fluid_properties/fluids/Methane.html.

[89] Bell IH. Water — CoolProp 7.2.0 documentation. 2025, URL: https://coolprop.org/fluid_properties/fluids/Water.html.

[90] Bell IH. ParaHydrogen — CoolProp 7.2.0 documentation. 2025, URL: https://coolprop.org/fluid_properties/fluids/ParaHydrogen.html.

[91] Brooks CJ, Wang W, Eyman DP. Supported transition metal catalysts for para- to ortho-hydrogen conversion. Technical Report, Iowa City: Iowa University; 1994, URL: https://ntrs.nasa.gov/citations/19950016832.

[92] Matsumoto M, Espenson JH. Kinetics of the interconversion of parahydrogen and orthohydrogen catalyzed by paramagnetic complex ions. J Am Chem Soc 2005;127(32):11447–53.

[93] Bhandari A, Rollings AP, Ratto L, Weinstein JD. High-purity solid parahydrogen. Rev Sci Instrum 2021;92(7):073202.

[94] Teschner T-R. Write your first CFD solver. 1st ed. Cranfield: CFD University; 2025, URL: https://cfd.university/learn/.

[95] Rusanov VV. The calculation of the interaction of non-stationary shock waves and obstacles. USSR Comput Math Math Phys 1962;1(2):304–20.

[96] Teschner T-R. Explicit vs. implicit time integration and the CFL condition. 2025, URL: https://cfd.university/learn/10-key-concepts-everyone-must-understand-in-cfd/explicit-vs-implicit-time-integration-and-the-cfl-condition/#aioseo-first-order-upwind-explicit.

[97] Toro EF. Splitting schemes for PDEs with source terms. In: Riemann solvers and numerical methods for fluid dynamics: A practical introduction. Berlin, Heidelberg: Springer Berlin Heidelberg; 2009, p. 531–41. http://dx.doi.org/10.1007/b79761.

[98] Teschner T-R. How to implement boundary conditions in CFD. 2025, URL: https://cfd.university/learn/10-key-concepts-everyone-must-understand-in-cfd/how-to-implement-boundary-conditions-in-cfd/.

[99] Fannelop TK, Ryhming IL. Massive release of gas from long pipelines. J Energy 1982;6(2):132–40.

[100] Richardson SM, Saville G. Blowdown of pipelines. In: SPE offshore europe. Aberdeen, United Kingdom: SPE; 1991, p. SPE–23070–MS. http://dx.doi.org/10.2118/23070-MS, URL: https://onepetro.org/SPEOE/proceedings/91OE/91OE/SPE-23070-MS/53036.

[101] Chen J, Richardson S, Saville G. Modelling of two-phase blowdown from pipelines—I. A hyperbolic model based on variational principles. Chem Eng Sci 1995;50(4):695–713.

[102] Richardson S, Saville G. Blowdown of LPG pipelines. Process Saf Environ Prot 1996;74(4):235–44.

[103] Webber DM, Fannelop TK, Witlox HWM. Source terms from two-phase fow in long pipelines following an accidental breach. In: CCCP international conference and workshop on modelling the consequences of accidental releases of hazardous materials. 1999.

[104] Cleaver R, Cumber P, Halford A. Modelling outflow from a ruptured pipeline transporting compressed volatile liquids. J Loss Prev Process Ind 2003;16(6):533–43.

[105] Allason D, Armstrong K, Barnett J, Cleaver P, Halford A. Experimental studies of the behaviour of pressurised releases of carbon dioxide. In: IChemE symp. ser. 2012, p. 142–52.

[106] Shargatov VA, Sumskoi SI, Pecherkin AS. Simulation of gas release from pipelines using a new numerical method based on the Godunov approach. J Phys: Conf Ser 2019;1205:012050.

[107] Newton A. Pipeline release rate model (PiRRaM) for pressure liquefied gases. In: IChemE hazards 32 conference. 2022, URL: https://www.icheme.org/media/19372/hazards-32-paper-02-newton.pdf.

[108] Newton A. An analytical solution to the transient one-dimensional compressible pipe-flow equations. In: IChemE hazards 34 conference. 2024, http://dx.doi.org/10.13140/rg.2.2.14007.64167, URL: https://rgdoi.net/10.13140/rg.2.2.14007.64167.

[109] Venkateshan S, Swaminathan P. Solution of algebraic equations. In: Computational methods in engineering. Elsevier; 2014, p. 155–201. http://dx.doi.org/10.1016/B978-0-12-416702-5.50004-1, URL: https://linkinghub.elsevier.com/retrieve/pii/B9780124167025500041.

[110] Tiselj I, Horvat A, Cerne G, Gale J, Parzer I, Mavko B, Giot M, Seynhaeve J, Kucienska B, Lemonnier H. WAHA3 code manual. JSI Report IJS-DP-8841, Liubliana: Jozef Stefan Institute; 2024, p. 186.

[111] Sokolowski L, Koszela Z. RELAP5 capability to predict pressure wave propagation phenomena in single- and two-phase flow conditions. J Power Technol 2012;92(3):150–65.

[112] Daude F, Galon P. Simulations of single- and two-phase shock tubes across abrupt changes of area and branched junctions. Nucl Eng Des 2020;365:110734, Publisher: Elsevier BV.

[113] Roache P. Fundamentals of verification and validation. 2nd ed. Socorro, New Mexico: Hermosa; 2009.

[114] Toro EF. The HLL and HLLC Riemann solvers. In: Riemann solvers and numerical methods for fluid dynamics: a practical introduction. Berlin, Heidelberg: Springer Berlin Heidelberg; 2009, http://dx.doi.org/10.1007/b79761, URL: https://link.springer.com/10.1007/b79761.

[115] Toro EF. FORCE fluxes in multiple space dimensions. In: Riemann solvers and numerical methods for fluid dynamics: a practical introduction. Berlin, Heidelberg: Springer Berlin Heidelberg; 2009, http://dx.doi.org/10.1007/b79761, URL: https://link.springer.com/10.1007/b79761.

[116] Sod GA. A survey of several finite difference methods for systems of nonlinear hyperbolic conservation laws. J Comput Phys 1978;27(1):1–31.

[117] Majumdar A. Generalized fluid system simulation program, version 6.0. 2013, http://dx.doi.org/10.13140/2.1.4804.0326, URL: http://rgdoi.net/10.13140/2.1.4804.0326.

[118] White FM. Chapter 9 compressible flow. In: Fluid mechanics. McGraw-Hill series in mechanical engineering, 7th ed. New York: McGraw-Hill; 2011, p. 642–59.

[119] Backus I. Github repository: Sod shock tube calculator. 2021, URL: https://github.com/ibackus/sod-shocktube.

[120] Celik IB, Ghia U, Roache PJ, Freitas CJ, Coleman H, Raad PE. Procedure for estimation and reporting of uncertainty due to discretization in CFD applications. J Fluids Eng 2008;130(7):078001.

[121] Brown GO. The history of the Darcy-Weisbach equation for pipe flow resistance. In: Environmental and water resources history. Reston, VA: American Society of Civil Engineers; 2002, p. 34–43. http://dx.doi.org/10.1061/40650(2003)4.

[122] Setzmann U, Wagner W. A new equation of state and tables of thermodynamic properties for methane covering the range from the melting line to 625 K at pressures up to 1000 MPa. J Phys Chem Ref Data 1991;20(6):1061–155.

[123] GL D. Phast: Software for consequence analysis. 2025, URL: https://www.dnv.com/software/services/plant/consequence-analysis-phast/.

[124] Wood AB. A textbook of sound. 3rd ed. London: Bell; 1955.

[125] Chen L, Specklin M, Khelladi S, Deligant M. An open-source solver for real gas compressible flows accounting for phase transition: Verification and validation. 2025, http://dx.doi.org/10.2139/ssrn.5377108, URL: https://www.ssrn.com/abstract=5377108.

[126] Batten P, Clarke N, Lambert C, Causon DM. On the choice of wavespeeds for the HLLC Riemann solver. SIAM J Sci Comput 1997;18(6):1553–70.

[127] Berry RA, Zou L, Zhao H, Zhang H, Peterson JW, Martineau RC, Kadioglu SY, Andrs D, Hansel JE. RELAP-7 theory manual. Technical Report, Idaho National Laboratory; 2018, URL: https://inldigitallibrary.inl.gov/sites/sti/sti/Sort_4964.pdf.

[128] Haar L, Gallagher JS, Kell GS. NBS/NRC steam tables thermodynamic and transport properties and computer programs for vapor and liquid states of water in SI units. Hemisphere Publishing Corporation,New York, NY; 1984, URL: https://www.osti.gov/biblio/5614915.

[129] Shu C-W, Osher S. Efficient implementation of essentially non-oscillatory shock-capturing schemes. J Comput Phys 1988;77:439–71.

[130] Shu C-W, Osher S. Efficient implementation of essentially non-oscillatory shock-capturing schemes, II. J Comput Phys 1989;83:32–78.

[131] Toro EF. High-order and TVD methods for scalar equations. In: Riemann solvers and numerical methods for fluid dynamics: a practical introduction. Berlin, Heidelberg: Springer Berlin Heidelberg; 2009, http://dx.doi.org/10.1007/b79761, URL: https://link.springer.com/10.1007/b79761.

[132] Brent RP. An algorithm with guaranteed convergence for finding a zero of a function. Comput J 1971;14(4):422–5.

[133] Lemmon EW, Bell IH, Huber ML, McLinden MO. Thermophysical properties of fluid systems. 2026, http://dx.doi.org/10.18434/T4D303, URL: https://webbook.nist.gov/chemistry/fluid/.

https://dspace.org/

A discontinuity-capturing approach to the simulation of two-phase hydrogen flows

Capmany, Nicolás; Könözsy, László Z.; Sanders, Drewan S.

2026-07-08
Elsevier
https://doi.org/10.1016/j.ijhydene.2026.155963
Capmany N, Könözsy L, Sanders D. (2026) A discontinuity-capturing approach to the simulation of two-phase hydrogen flows. International Journal of Hydrogen Energy, Volume 249, July 2026, Article number 155963

Downloaded from a DSpace repository. https://dspace.org/